Current State of Models for the Prediction of Mechanical Failures in Solid Oxide Fuel Cells

Arata Nakajo, Jan Van herle and Daniel Favrat

1 Introduction

The solid oxide fuel cell (SOFC) technology has to face many challenges before its large-scale commercialisation. Cost reduction, along with enhanced reliability, durability, fuel flexibility, load following capabilities and compactness are needed. Yet, despite all the research, the exact underlying mechanisms of the electrochemical reactions have not yet been unambiguously identified. The high-temperature environment promotes physicochemical modifications of the materials that alter the electrochemical and mechanical properties after prolonged use. The driving forces of these degradation processes that arise from chemical interactions between the SOFC materials themselves, on the one hand, and the volatile contaminants transported by the fed gases, on the other hand, have not yet been fully clarified.

The structural reliability of SOFCs is a salient issue. The end of operation of a stack is ultimately caused by the loss of structural integrity of one or several of the cells. This is the result of (i) the accumulation during operation of physicochemical alterations, of plastic and creep deformations, and (ii) the modification of the temperature profile, due to the degradation of the electrochemical performance of the cells. Mechanical issues do not, however, exclusively occur after prolonged use. Inappropriate control during load following, harsh conditions and thermal cycles can induce discrete failures. The in-series

A. Nakajo (✉) · J. Van herle · D. Favrat
Laboratoire d'Energétique Industrielle (LENI),
Ecole Polytechnique Fédérale de Lausanne (EPFL),
Bat. ME A2, Station 9, 1015 Lausanne, Switzerland
e-mail: arata.nakajo@epfl.ch

J. Van herle
e-mail: Jan.Vanherle@epfl.ch

D. Favrat
e-mail: daniel.favrat@epfl.ch

assembly of the standard repeating units (SRU) in a stack is a striking weakness, the mitigation of which is hindered by the complexity of the failure modes in the ceramic materials. Mechanical failure in a single cell induces a succession of detrimental effects that act in a coupled manner. For instance, delamination or cracking of the electrode layers breaks the ionic and/or electronic conduction paths to the electrochemical reactions sites. The ensuing local loss of performance induces a harmful redistribution of the current density. Once cracked, the electrolyte or sealant does not any longer ensure the separation of the fuel and air compartments to the fullest extent. The local and unsteady combustion provokes a local increase of the temperature, as well as diverse chemical alterations of the cell layers. All these undesirable phenomena promote in turn additional stresses, which reach critical values in an accelerated manner. The SOFC field is, therefore, characterised by strong interactions between the phenomena.

Despite the evidence of mechanical issues in SOFCs, which are experienced even during laboratory button cell tests, this topic is still receiving limited attention. Efforts are seen as stand-alone tasks, owing to the different experimental and modelling techniques needed to gather the essential information, whereas mechanical failures in SOFCs are likely intricately related to physicochemical and electrochemical aspects.

This survey of the current state of models for the prediction of mechanical failures in SOFC stacks comprises five parts. For conciseness, the emphasis is on planar stack design with anode-supported cells. The description can be easily transposed to other situations, differing in terms of type of cell, geometry or operating temperature. In Sect. 2, the diverse origins of stress in the components are briefly presented, along with the most common failure mechanisms. In Sect. 3, a brief overview of the mechanical behaviour of the cell, sealing and gas diffusion layer (GDL) materials is provided, in the view of their implementation in numerical tools based on the finite-element method (FEM). The need for the complete temperature and ageing dependences and refined constitutive laws for rate-independent plasticity and creep is highlighted. Section 4 presents the modelling approaches applied at the SRU scale and discusses the particularities of SOFC modelling: (i) initialisation steps, (ii) boundary conditions representative of stacking of the repeating units and (iii) choice of suitable elements among those available in commercial FEM tools. The discussion is enlarged with (i) simple models, such as derived from the beam theory, and (ii) the recent representative elementary volume (REV) analyses that may provide, in the future, insights into the failure modes. Section 5 illustrates the current modelling capabilities at the SRU scale with studies available in the literature. To conclude, the most stringent model improvement needs are discussed in Sect. 6.

2 Origins of Stresses and Mechanical Failures in SOFC Stacks

Multilayer systems are extensively used in engineering to fulfil combined requirements on different aspects, be it mechanical, electrical or thermal. A planar SOFC stack is a typical example, at different scales. To build a functional unit, the

impervious electrolyte, interconnects and sealants achieve the separation of the air and fuel compartments, whereas the in-series electrical stacking of the SRUs further requires the use of GDL. The mechanical interactions between these components depend on the selected technological solutions. Most of these parts are themselves multilayer systems.

In broad terms, the nature and long-term evolution of the stress is governed by the properties of the materials. Similar to other energy conversion devices, SOFC stacks will incur repeated full or partial thermal cycles and variations of the electrical load, which reduce the lifetime. An essential mitigation approach is to ensure reduced or suitable differences between the coefficients of thermal expansion (CTE) of the different materials. This is usually completed by the wise use of compliant linking elements to accommodate the mismatch strains that cannot be avoided. Because of the temperature-dependence of the CTE and the several manufacturing steps of a stack, such as cell sintering, metallic interconnect (MIC) coating, sealing and reduction procedure of the nickel-based anode, this task is not straightforward. In a next step, the understanding and control of irreversible deformation alleviates the history-dependent degradation of the behaviour. Here, a comprehensive analysis must include together electrochemical and mechanical aspects (see Sect. 6).

The following description of the origins of stresses and failure mechanisms per component is not exhaustive, because of their dependence on the choice of the technological solutions and geometry of the components. A classification of the mechanical failures in SOFC stacks developed in Japan is available [46]. Figure 1 depicts some of the common failures observed during experiments.

2.1 Cell

The cell or membrane electrode assembly (MEA) is the central component. It comprises the electrolyte, the electrodes as well as the contacting and required compatibility layers. As any multilayer system made of brittle materials, the MEA is prone to failures related to residual stresses ensuing the manufacturing process, and to further thermal cycling and prolonged exposition to aggressive environments [23]. The electrochemical performance is the first requirement that dictates the choice of the materials and the microstructure. The selection has to be performed in the view of long-term performance to alleviate undesirable chemical reactions and morphological alterations of the microstructure promoted by the high-temperature aggressive environment [47, 68, 80, 109, 118]. This is therefore a trade-off, as high electrochemical activity and chemical stability are usually contradictory aims.

Stresses in a cell embedded in a stack originate from different phenomena. Residual stresses build up during the cool down, after the sintering, because of the mismatches between the CTEs of the materials of the cell. The dissymmetry of the system results in curved specimens. Stresses in the cell then arise from mechanical

load due to the stacking and the joining with the other components of the SRU. The reduction of nickel oxide in the anode takes place when fuel is fed for the first time and results in a change in porosity, hence in mechanical properties, and shrinkage [99, 102]. During operation, the uneven distribution of temperature and oxygen vacancy concentration in the layers prone to isothermal expansion, cause additional stresses in the cell [105]. In the long-term, the progressive physico-chemical alterations, creep mainly governed by the temperature and stress profile, and the possible shrinkage of the ceramic materials during thermal cycles [82, 84], can induce history dependences that reduce the resistance against load following and thermal cycling.

The cracking modes in the MEA layers and at the interfaces depend on the design, which consists in the choice of a supporting layer and of materials of suitable CTE. They may evolve during combined cycling and ageing because of the relaxation of the initial shielding compressive stress in the weakest layers [91]. Lanthanum strontium manganite (LSM) has been used for a long time and has proved its stability during operation at high temperature. The use of a composite LSM–yttria-stabilised zirconia (YSZ) electrode enables a considerable improvement of the performance, hence reduction of the operating temperature. Lanthanum strontium cobaltite ferrite (LSCF) cathodes combined to yttria (YDC) or gadolinia-doped ceria (GDC) compatibility layers are the result of concurrent research on more active materials. In an LSM-based cathode deposited on an Ni-YSZ/YSZ anode-support, the stress can change from tensile to compressive, depending on the temperature, whereas an LSCF cathode withstands tensile stress. In the former case, buckling-driven delamination is observed at the interface with the electrolyte [98], whereas cracking of the LSCF cathode may occur [70]. The same issues affect the contacting layers, as shown in Fig. 1. The cracking modes in the Ni-YSZ anode on an electrolyte support exhibit similarities with the latter case. Once at the interface, perpendicular cracks can either further propagate in the support, continue along the interface, or kink [23].

2.2 Interconnect

Structural issues related to the interconnect depend on the choice of the material. High-temperature SOFCs, such as the tubular design of Siemens-Westinghouse [111], make an exclusive use of ceramic materials, apart from the nickel felt used for current collection. The most common material, lanthanum chromite, is brittle and prone to non-uniform isothermal expansion when simultaneously subjected to reducing and oxidising atmospheres on different faces [131].

The decrease of the operating temperature pursued by the anode-supported cell technology enables the use of metallic components, with beneficial implications on costs and design possibilities. Similar to the MEA, an MIC is a multilayer of finite durability [66] wherein, in state-of-the-art solutions, a ceramic coating slows the growth of the oxide scale of lower electrical conductivity and the evaporation of volatile chromium species that contaminates the cathode. At the microscale, the
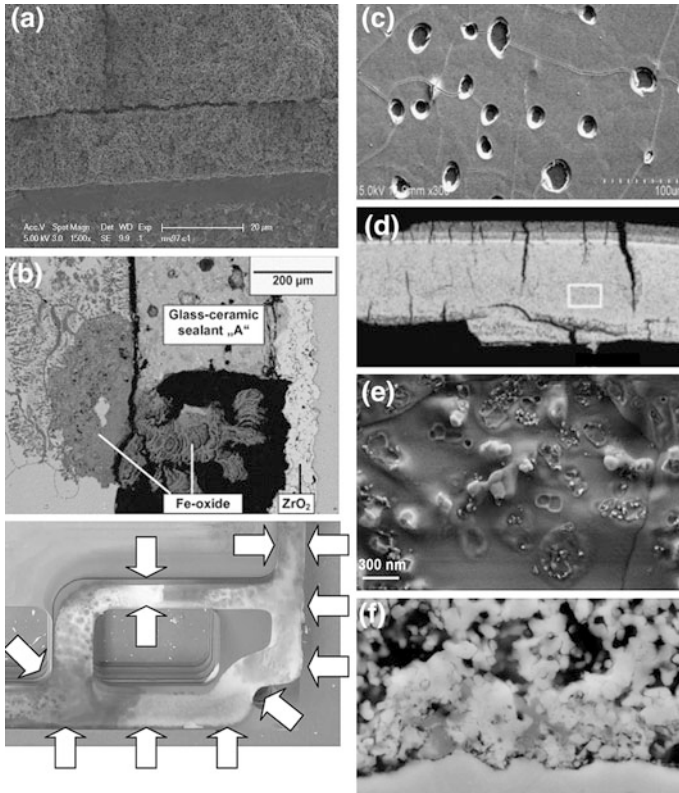
Fig. 1 Examples of mechanical failures and microstructural alterations observed in SOFC stacks. **a** Delamination of cathode current collection layer [21], reproduced here with kind permission from © ASME 2008. **b** cracking of the sealant [10], reproduced here with kind permission from © Elsevier 2006, and loss of gas-tightness [72], reproduced here with kind permission from © John Wiley and Sons 2009. **c** MIC coating delamination [18], reproduced here with kind permission from © Elsevier 2008. **d** anode support reoxidation cycling [25], reproduced here with kind permission from © Elsevier 2009 **e** formation of zirconates in LSM–YSZ cathode [68], reproduced here with kind permission from © Elsevier 2009. **f** chromium deposit in LSM–YSZ cathode [78], reproduced here with kind permission from © The Electrochemical Society 2007

evolution of the thickness of the layer, coupled to creep and/or rate-independent plasticity, has a strong impact on the nature of the mechanical failures, which exhibit similarities with those acting in thermal-barrier coatings (TBC) of gas turbine blades [24]. Spallation and delamination is experimentally reported [18] (see Fig. 1).

While ductility is an advantage for the manufacturing of complex shapes, structural issues can arise from irreversible deformation generated during operation, as thermal stresses can exceed the elastic limit at distinct locations in the SRU [60, 88, 89, 93]. Cracking of the MIC is seldom observed. In contrast, the creep and increments of plastic strain generated during discrete events and prolonged

use, respectively, can progressively lead to cell failure, through buckling, loss of electrical contact or gas-tightness [88, 89, 93]. The creep strain rates in these materials under the stress and temperature of operation is higher than those of the cell [86]. The expected temperature differences of 100 K over the SRU [92] induces very different amounts of irreversible strains in the zones subjected to comparatively high or low temperatures. The need to reduce the thickness of the components to decrease the costs and the thermal inertia of the stack increases the difficulty to prevent such failure modes. As classical stability issues are progressively solved, the contribution of the oxide scale and coatings to the mechanical behaviour of the component will increase.

2.3 Sealants

The sealing solutions span, with increasing level of mechanical interactions between the joined components, from compressive gaskets [13] to glass-ceramic materials [27], through thin metallic elements [127].

The main advantage of compressive gaskets is their compliance, which at first sight, should ease the requirements during the development of an SOFC stack to ensure the integrity of the cell. A loading system is needed to apply a high assembly load. It induces additional complexity, hence weakness, and weight which is not suitable for mobile applications. The ensuing compressive stresses further place tighter requirements on the dimensional tolerances of adjacent SRU components to avoid cell cracking caused by flatness imperfections. Despite the lack of mechanical characterisation (see Sect. 3), the properties of the compressive gasket materials certainly change after the first heat-up and differ depending on the atmosphere. An improper assembly process, the lack of stability of the matting surfaces and of the compressive load can cause the cracking of the gasket. However, the most deleterious structural effects arise from the slightly permeable nature of this sealing solution, which can indirectly induce cell failure, through parasitic combustion and, in the worst case, partial and unsteady reoxidation of the Ni in the anode and reduction of the cathode material [128].

Rigid sealants are alternatives to compressive gaskets. They can be divided into four main categories [28]: glass [14, 35], glass-ceramic [79, 110], metal brazes [54, 123] and bonded-compliant seals (BCS) [125]. All of them are more hermetic than compressive gaskets, at the cost of increased development efforts. They yield stronger mechanical interactions between the different components of the SRU, hence importance of CTE mismatches. A compliant component, such as the metallic foil in the BCS concept, can alleviate the ensuing stress in the cell. Cost and increased flexibility in shape are additional advantages over compressive gaskets, in particular for glass-based sealants, which can be dispensed either by a syringe as a paste or placed on the sealing surfaces as tape cast sheets. Their dense nature and adhesion to the other SRU materials spares the development, weight and price of a compressive loading system. This advantage may be decisive for

mobile applications, where dynamic issues related to the application of the mechanical load can arise. The mechanical properties of a glass-ceramic sealant in a stack are expected to exhibit disparities. They depend on the sealing procedure performed on the whole stack, during which completely uniform conditions are impossible to ensure (see Sect. 3).

The composite and evolving structure of the ceramic-glass sealants as devitrification proceeds induces microvoids, which can be possibly healed at operating temperature [95]. The most common failure mode of a glass-ceramic sealant is cracking in the bulk of the sealant or at the sealing interfaces, during thermal cycles. The strength of the interfaces with the sealing areas may suffer from direct or indirect deleterious chemical interactions [17].

2.4 Gas-Diffusion Layer

The variety of mechanical failures related to GDLs is considerable, because solutions are specific to stack manufacturers. These are, most of the time, proprietary, which accounts for the scarce available data. In the case of metallic foams, large cracks in the GDL are unlikely thanks to the usually compressive stress state. The impact of corrosion on the global mechanical behaviour of metallic foams is expected to be severe in comparison with the MIC case because of the thickness of the struts relative to the oxide scales. GDLs can cause cell fracture indirectly. Partially sintered pastes are extensively used to enhance the electrical contact, mitigate the release of volatile poisoning species and slow the growth of oxide scales. They result in weak adhesion between the GDLs and neighbouring elements [20]. The initially designed CTE mismatch, adjusted by consolidation steps to control the stress state and the distribution of the contact pressure on the different components, may be altered by non-uniform creep deformation generated during prolonged operation. The possible ensuing change in stress state during thermal cycles can induce localised losses of electrical contact. Slight differences in relative density, combined to the limited number of struts in the thickness can significantly alter the creep strain rate at high temperature [97]. They affect the uniformity of the gas supply in a stack and, at a smaller scale, the gas flow distribution within the stacked SRUs. This results in accelerated degradation hence increased risks of mechanical failures [90].

3 Materials

The limited knowledge on the essential mechanical properties of the SOFC stack materials and, further, on their evolution during prolonged and cycling conditions, induced by the interplay with physicochemical phenomena, hinders the efficient mitigation of mechanical failures. A brief overview of the properties of the most

common materials is provided here. The reader is redirected to compilations on the mechanical properties of SOFC materials available in the literature for more extensive information [7, 86, 90, 106, 120]. The data summarised here are detailed in [86, 90].

3.1 Coefficient of Thermal Expansion

The CTEs of SOFC materials are available for a broad variety of compositions in different atmospheres. The thermal expansion contains a chemical contribution, depending on the environment. Considerable stress and significant ensuing deformation in the SRU can arise from chemical (isothermal) expansions.

Most of the CTE data consists in values for a single temperature difference, typically room temperature (RT) to 1273 K. In comparison, few temperature-dependent or differential values are readily available, despite their importance for a comprehensive stress analysis. The thermal expansions between the reference state and those of interest, i.e. sintering and the temperature of operation, anode reduction, heat treatment of the glass sealant and room temperatures at least, have to be known. The implementation of thermal expansion in commercial FE software is straightforward. It requires either the differential or total CTE from a reference state [1], and can be easily controlled by field variables or dedicated subroutines. Expansion or shrinkages can be modelled by using swelling procedures. Figures 2 and 3 depicts the typical temperature dependence of the CTE of the materials.

The most common electrolyte material is YSZ. Another central one is yttria- (YDC) or gadolinia-doped ceria (GDC). Despite its higher ionic conductivity than 8YSZ, its drawback are non-negligible electronic conduction at low oxygen partial pressure and isothermal expansion. It can also serve as a compatibility layer, to prevent undesirable reactions between the YSZ electrolyte and an LSCF cathode. The CTEs of both materials exhibit temperature dependence. SRU typically have to withstand spatial temperature differences of 100 K, e.g. 973–1073 K. The corresponding variation of the CTE between RT and 1073 K in one data set is of approximately $9.8-11.0 \times 10^{-6} \, \text{K}^{-1}$ for 8YSZ and $12.1-12.9 \times 10^{-6} \, \text{K}^{-1}$ for GDC, which can lead to imprecision in the calculation of the stress field.

Ni-based cermets are preferred for SOFC anodes owing to their good electro-chemical activity for H_2 and CO oxidation, and catalytic activity for the reforming of hydrocarbons. The ionic conducting phase is made of YSZ or GDC. The CTEs of Ni-YSZ anodes in oxidised and reduced state increase for higher NiO or Ni contents. The most striking feature is the anomaly due to the antiferromagnetic to paramagnetic transition of NiO (approx. 530 K), and the ferromagnetic to para-magnetic transition of metallic Ni (approx. 630 K), which entails a change in the structure from rhombohedral to cubic structure in the case of NiO. The CTE between RT and 1073 K is comprised within $11.2-13.3 \times 10^{-6} \, \text{K}^{-1}$ [44, 84, 100]. Particular attention is required for composites materials subjected to thermal cycling. In such conditions, Mori et al. [84] report a more severe increase of the CTE of Ni-YSZ material with increasing heating/cooling rates and denser samples.

Fig. 2 Dependence on temperature of the CTE (*right*, *r*) and Young's modulus (*left*, *l*) of MEA materials, from the data compiled in [87, 91]. Reproduced here with kind permission from © John Wiley and Sons 2011
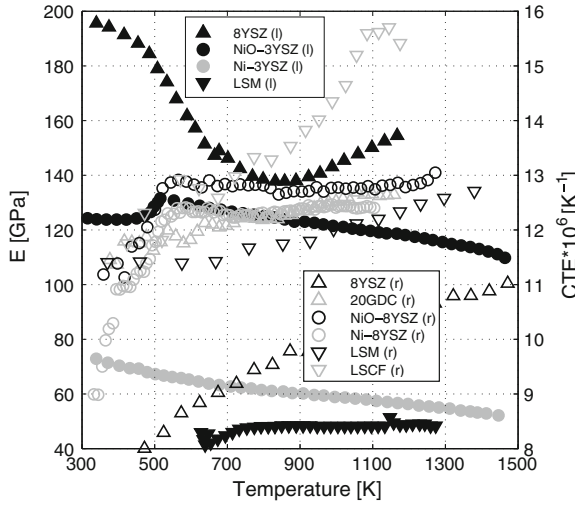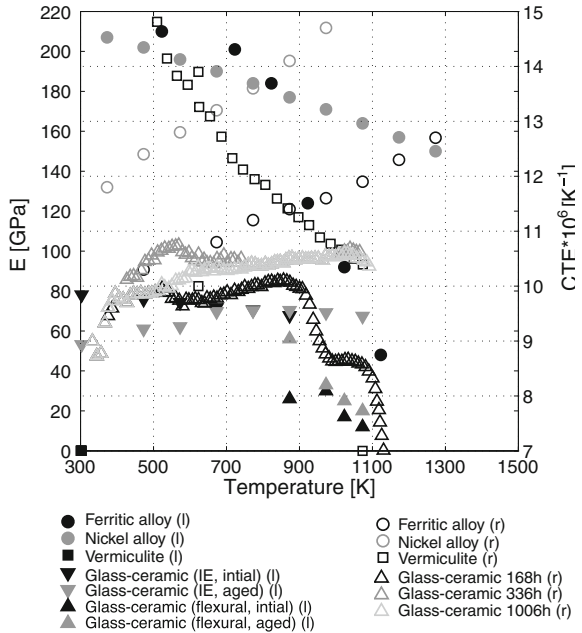

Fig. 3 Dependence on temperature of the CTE (*right*, *r*) and Young's modulus (*left*, *l*) of sealing and MIC materials, from the data compiled in [86]

The effect is larger during the first 5–10 cycles, approximately 4.67×10^{-8} and 5.75×10^{-8} per cycle for $2\,\mathrm{K\,min^{-1}}$ and $10\,\mathrm{K\,min^{-1}}$ heating ramps, respectively, between 323 and 1273 K. It then reduces to 4.28×10^{-9} and 5.5×10^{-9} per cycle. The difference between cooling and heating measurements indicates a shrinkage of the anode. Sun et al. [112] report a similar value of 1.2×10^{-8} (1.4×10^{-8} on

average for [84]) for cycling between 298 and 1173 K. To our knowledge, the exact origin of this behaviour has not yet been clarified.

The CTE of LSM ($11.6-13.2 \times 10^{-6}\,K^{-1}$, between RT and 1073 K) closely matches that of YSZ or the anode, whereas that of LSCF is higher ($13.0-19.3 \times 10^{-6}\,K^{-1}$, between RT and 1073 K). These CTEs can be tailored, to some extent by modifying the content of Sr on the A-site of $La_{1-x}Sr_xMnO_3$ [83], respectively the Sr and Fe content on the A- and B-site of $La_{1-x}Sr_xCo_{1-y}Fe_yO_3$ [115, 116]. Porous $La_{0.6}Sr_{0.4}MnO_3$ samples undergo severe shrinkage during thermal cycling but not ageing in air or oxygen between 873 and 1373 K [83]. The strain per cycle is as high as 5×10^{-4}.

Most of the mechanical data on rigid sealants concerns the so-called G18, a barium-calcium-aluminosilicate (BCAS) glass-ceramic material ($35BaO - 35SiO_2 - 15CaO - 10B_2O_3 - 5Al_2O_3$, mol%) developed at the Pacific Northwest National Laboratory [76, 110]. Data on reactive air braze can be found in [39, 48, 54, 123, 124, 126]. The addition of boron oxide is a means to decrease the glass transition temperature, control the viscosity and improve the wetting of BCAS ceramic-glasses [28], while that of alumina modifies the rate of crystallisation. The sealing procedure for G18 yields a content of crystallite phase of about 50 vol.%, which increases up to 70 vol.% after 120 h at 1023 K and then stabilises [76]. The CTE between RT and 1073 K is in the range of $9-13.0 \times 10^{-6}\,K^{-1}$ depending on the composition [79].

Compressive gaskets for high temperature applications are usually made of either vermiculite, phlogopite mica or muscovite mica. Exfoliation results in highly compliant structures made of crystal platelets or fine particles. The CTE of such materials is likely very complex and its measurement challenging. Depending on the manufacturing process, an orthotropic behaviour is expected. The scarce available data indicates that it lies within $10-14 \times 10^{-6}\,K^{-1}$ between RT and 1073 K [34].

Preliminary selections retained two main classes of metallic alloys, ferritic and nickel-based chromia-forming alloys [133]. The ferritic alloys have a significant edge on the costs. Most of the initial developments focused on the improvement of the long-term electrical conductivity, mitigation of the volatilization of chromium and CTE adjustments. The typical CTE of chromia-forming ferritic alloys ($11.3-11.9 \times 10^{-6}\,K^{-1}$, between RT and 1073 K) matches that of the anode, whereas that of nickel-based alloys is higher ($15.2 \times 10^{-6}\,K^{-1}$). In both cases, element addition can reduce the mismatch with the anode, electrolyte or cathode materials, depending on the supporting layer and desired stress state in the components.

3.2 Elastic Properties

Different procedures exist for the measurement of the elastic properties. An evaluation of four different techniques is provided in [103], the most common being the impulse excitation technique (IE).

The Young and shear moduli strongly depend on the porosity. A word of caution should be warranted on the use of Young's modulus as an indicator of the presence of microcracks. This approach considers that the decrease of the effective area that can sustain mechanical loads, due to the presence of cracks, results in a decrease of the apparent Young's modulus. While its justification seems straightforward, care is required when using such an approach. Indeed, depending on the fracture toughness of the material, the simplest case, i.e. a unique slender crack in a dense sample, highlights that the crack length which significantly affects the apparent Young's modulus can be far larger than that would have induced failure. The implementation in commercial software of a linear elastic behaviour is straightforward. Figures 2 and 3 depict the typical temperature dependence of the Young's modulus of the materials.

The reported stress–strain curves of YSZ samples are linear over the investigated temperature range [2, 49]. The Young modulus exhibits a strong temperature dependence, whereas, in addition, that of GDC decreases by 80 % at an oxygen partial pressure of 10^{-20}, compared with air [40, 121]. In air, the values are comparable for both materials and range from 140 to 220 GPa for dense samples.

The reduction procedure entails an increase in porosity of the Ni-based anode material, which is well predicted by simple relations [102, 106]. Data on the temperature dependence of the Young's modulus of the common compositions of Ni-YSZ anodes remain scarce, but reported trends are fairly similar [11, 73, 100]. The Young's modulus in oxidised state exhibits a peak related to the antiferromagnetic to paramagnetic transition of NiO, already reflected in the CTE, followed by a decline, though a shift in temperature appears when comparing data between [100] and [11]. Because of the possible differences in porosity, typical values lie in the range of 80–170 GPa (oxidised state) and 30–100 GPa (reduced state).

The data on the elastic properties of cathode SOFC materials is very scarce. Moreover, most of the measurements are performed on dense samples, which differs from the porous microstructure of a functional cathode. The Young's modulus of LSM samples measured by Giraud et al. [33] exhibits singularities. IE measurements could not be performed for temperatures lower than 623 and 873 K for porous and dense samples, respectively, presumably because of their ability to absorb vibrations. To our knowledge, no explanation has been provided for this behaviour. For a porosity of 4–29 %, the Young's modulus ranges from 48 to 120 GPa.

The Young modulus of ferritic alloys for SOFC application drops from 220 to 50 GPa, by increasing the temperature from RT to 1073 K. That of Ni-based alloys degrades significantly less, i.e. around 150 GPa at 1073 K.

At first sight, the mechanical behaviour of metallic foams appears as the simplest among competing GDL solutions, as their structure offers homogenised properties. This is only partially achievable, however, due to their non-periodic structure and the effect of the number of struts [8]. Non-negligible anisotropy, non-uniform deformation patterns and considerable scatter in the measurements of identical samples are reported [8, 96]. Nevertheless, simple relations based on analytical considerations on the possible deformation modes of simplified unit

cells provide correct scaling relations for the qualitative prediction of some properties of cellular solids deduced from those the dense material, e.g. [32], depending on the relative density.

Stress–strain curves of G18 exhibit large differences among samples from similar laboratory batches, which underscore the sensitivity of the mechanical properties to processing. The measurements of the Young's modulus from bend test and IE technique differ drastically and nonlinear behaviour occurs above 973 K, because of significant irreversible deformation. Liu et al. [65] propose a relation for the prediction of the time- and temperature-dependent Young's modulus of BCAS glass-ceramic material. The values gathered by IE are in the range of 50–80 GPa [110].

The mechanical behaviour of compressive gaskets is very complex and likely depends on the environment [13, 34].
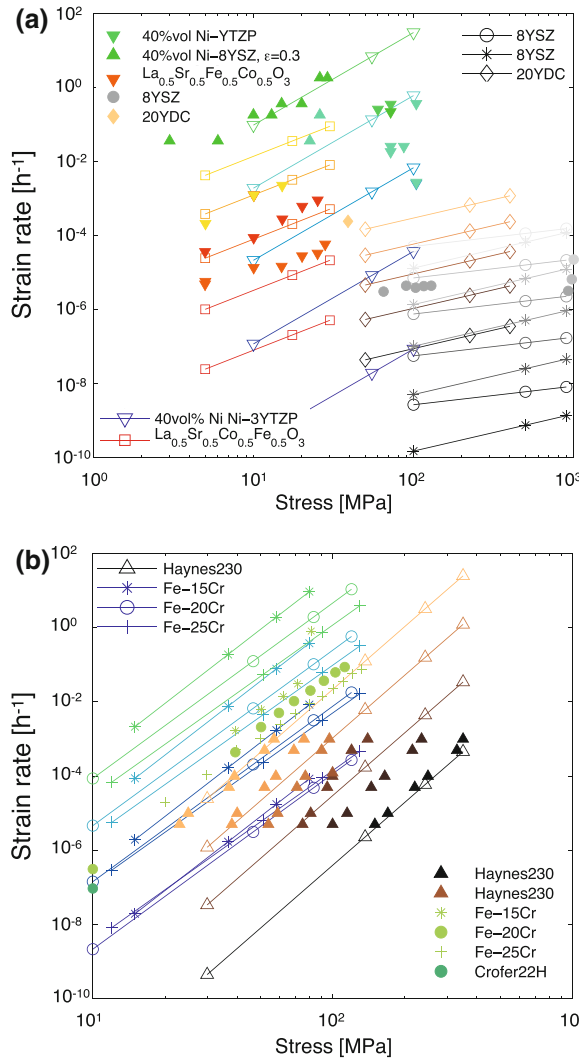
3.3 Rate-Independent Plasticity and Creep

Unified equations that couple rate-independent plasticity and creep [114] are not readily available for SOFC materials. The data in the literature allows a simple description that arbitrarily separates the two contributions. In the case of isotropic hardening FEM tools for structural analysis conveniently accept data in the form of tabular data that describes the plastic strain–stress relation for uniaxial loading. This approach suffers limitations, in terms of maximum allowed strain, typically 10 %, predictions in the behaviour during cycling and validity for stress states characterised by large rotations of the principal axes.

Creep occurs when the material is loaded at a temperature near one half of its melting point and can be classified into three main categories, depending on the mechanism: diffusion, viscous and dislocation creep, as shown in deformation mechanism maps [4]. Difficulties arise from the temperature dependence and possible overlapping or changes in the dominant mechanism. In the case of SOFC materials, most of the existing measurements are at temperatures significantly higher than those encountered during normal operation of SOFC stacks. The needed extrapolation can lead to seriously misleading predictions. In general, creep in polycrystalline metals loaded at SOFC operating temperature occurs by grain boundary sliding and diffusion at low stress, while higher stresses are in the regime of thermally activated climb or glide dislocation motion [4].

The evolution of the strain rate during a tensile creep experiment under constant load usually exhibits three regimes: a fast initial deformation, followed by a constant strain rate and a final increase of the strain rate before failure, referred to as primary, secondary and tertiary creep. Most of the data focuses on the second regime. For preliminary investigation, it can be recast in the form of the Norton law. Figure 4 depicts a comparison of experimental creep strain rate and predictions from calibrated Norton law, on the typical range of stress and temperature in an SOFC stack during operation.

Fig. 4 Comparison between computed (*lines*) and measured (*symbols*) creep strain rates of **a** MEA and **b** MIC materials [86, 90]. Reproduced here with kind permission from © Pergamon 2012

The separation of the contributions of rate-independent plasticity and creep can lead to inconsistent interactions. ABAQUS [1], for instance, properly handles isotropic creep and plasticity together. In the case of either anisotropic plasticity or creep, plasticity is not accounted for in creep simulations.

The investigation on the creep behaviour of the ceramic materials is limited. Data on bending creep of 8YSZ and 20YDC in a temperature range of 1223–1563 K and 1323–1398 K, respectively, is available in [42, 55, 69]. The creep strain rate in the anode is the highest among the cell layers, in their respective expected stress range. It is, therefore, expected to dominate that of anode-supported cells, for geometrical and material reasons, but studies on the

topic are scarce [37, 81]. The data found on the bending creep behaviour of LSM materials is not relevant for simulations of SOFC operation, since it is limited to the high-temperature domain, around 1523 K [104]. For $La_{0.5}Sr_{0.5}Fe_{0.5}Co_{0.5}O_3$ measurements at 1173–1323 K in air are available [59].

The maximum elongation before rupture of metallic alloys is high, typically around 20–60 % [41, 119]. The engineering stress–strain curves can be used to estimate those of the metallic GDLs.

For the glass-ceramic sealant, Nguyen et al. [95] propose a refined continuous damage model for dealing, in an homogenised manner, with viscoelastic behaviour and plasticity of the glass phase, microcracking, void formation and decohesion at the interfaces between glass and crystallite phases. A simpler approach is to implement the nonlinear curves in FEM software, with a hypoelastic constitutive relation, and complete these with a simple expression for the creep [110].

The behaviour of high-temperature compressive gaskets is complex. The results from Bram et al. [13] show a fairly reproducible response after the third loading cycle for vermiculite and mica-based compressive gaskets. Their data, however, is not sufficient for structural analysis at the SRU scale which requires the knowledge of the behaviour of the gasket for different loading and unloading paths [12].

3.4 Strength of Brittle Ceramic Materials

The strength of SOFC ceramic materials is not an intrinsic property, but strongly depends on the flaws and defects, that result from the manufacturing process and act as stress concentrators. Their failure stress is statistically distributed as a function of the flaw size distribution and depends on the size of the component. The Weibull analysis [122] is based on the weakest-link model, with an infinite number of links, the weakest one controlling the strength. The classical two-parameter version is valid for one defect population. The preferred test method is the ring-on-ring arrangement which generates a biaxial stress field and tests a larger volume [53]. Table 1 summarises the range of reported characteristic strength, Weibull modulus and reference volume [86]. The Weibull modulus is usually lower than 10, which is the threshold for technological ceramics. For the anode, the amount of data on the strength in the most relevant conditions, i.e. at high temperature and in reduced state, is limited because of the required testing apparatus and efforts.

.Data on the effects of cycling and ageing on the strength of ceramic SOFC materials is limited and contradictory. The decrease of ionic conductivity of YSZ during ageing is well known, though the mechanisms have not yet been unambiguously clarified [3, 38, 50–52]. Among the possible causes of this phenomenon, the cubic to tetragonal phase transformation is expected to have implications on the mechanical behaviour. This is confirmed by the measurements of the tensile strength of 8YSZ samples aged in air at 1273 K for 1000 h by Kondoh et al. [49]. In contrast, studies do not show any significant improvement in similar conditions [69]

Table 1 Example of Weibull parameters of SOFC materials

		Characteristic strength (MPa)	Weibull modulus	Reference volume[a] (mm^3)	
Cathode	RT	52	6.7	1.22	[7]
(LSM)	1073 K	75	3.7	2.84	[7]
Electrolyte	RT	232	5.7	0.54	[7]
(YSZ)	1073 K	154	8.6	0.30	[7]
Anode[b]	RT	290 (277,304)	6.8 (5.4,8.6)	10.11	[86]
(NiO-YSZ)	1073 K	253 (242,266)	6.6 (5.2,8.4)	10.69	[86]
Anode[c]	RT	97.6 (86.4,110.2)	4.3 (2.9,6.4)	9.55	[102]
(NiO-YSZ)	1073 K	–	–	–	
Anode[d]	RT	79 (73,85)	7 (5,10)	4.81	[102]
(Ni-YSZ)	1073 K	–	–	–	
Compatibility layer	RT	134	3.8	1.03	[7]
(GDC)	1073 K	183	5.7	0.58	[7]

[a] Computed afterwards in compliance with ASTM C1499 standards [30]
[b] Porosity of 25 % after reduction
[c] Porosity of 18 %
[d] Porosity of 36 %

or only decreased Weibull modulus [53]. Similarly, the strength of anode materials can decrease during thermal cycling. The literature, however, exhibits opposite observations [73]. Extensive research to find the exact underlying phenomena and causes of these discrepancies has not yet been performed.

Data on the strength of cathode materials mostly consists in flexural bending strength, predominantly for dense materials. Values of the Weibull parameters are seldom found. The data on LSM from Atkinson et al. [7] is one of the few available. Surprisingly low Weibull moduli are reported, without explanation and similar to GDC, the characteristic strength increases with temperature. The low-temperature plastic deformation of LSM samples observed by Cutler et al. [77] is accompanied by a low Young's modulus and bending strength. These results contrast with the higher strength and brittle behaviour measured by De Souza et al. [22] for $La_{0.875}Sr_{0.125}MnO_3$.

3.5 Additional Information

Additional information is needed for structural analysis, depending on the stack technology, the modelling approach and the problems to solve, because of the several manufacturing steps. Section 4 provides the details of the model implementation.

The reduction procedure induces a change of the mechanical properties and, in most cases, a slight shrinkage of the anode. Most of the data on the reduction strain is available in studies of the redox behaviour of anode supports. Pihlatie et al. [99] have proposed a model to predict the cumulative redox strain (CRS). The underlying

phenomena of the dimensional change include chemical expansion, rate-independent plasticity, creep and possibly microcracking. The dependence on the reduction conditions, such as temperature and humidity, anode microstructure and cell geometry is recognised [36, 101], but considerable discrepancies exist among the measurements. The largest strain value of -2.34×10^{-2} exceeds the contribution of the typical pursued CTE mismatch between SOFC materials which lies between 10^{-3} and 10^{-2}.

The use of a glass-ceramic material implies additional manufacturing steps which have to be performed on the whole SOFC stack before operation, as the sealants are assembled in the form of paste or tape cast sheets. A typical sequence starts with the burn-off of the binder. The amorphous glass must then flow sufficiently to accommodate initial dimensional irregularities and effectively wet the sealing surfaces above the glass transition temperature (around 850–1010 K), approximately equivalent to the softening point (around 900–960 K) [28]. At the same time, excessive overflow must be avoided for structural integrity. The glass then partially devitrifies during the heating ramp and subsequent heat treatments. A proper control of the final amount of crystallite phases results in sealants of suitable strength and CTE, to alleviate the residual stresses caused by the stronger joining of the SRU components. The key properties of the material, i.e. glass transition and/or softening temperature, crystallization kinetics, viscosity, CTE and strength are interrelated and adjustable by modifications of the composition. The reported ideal sealing temperature of G18 is 1123 K, and effective joining of the materials requires some compressive load [76]. This must be included in the initialisation procedure before the structural analysis (see Sect. 4).

Very few studies have focused on the contact behaviour between the GDL, the cell, the compressive gaskets and the interconnect. The nature of the contact and the friction coefficient, if relevant, are unknown. The values of the former used in stress analyses are guesses, between 0.16 and 0.2 [15, 92]. Some data exists on the strength of the interface between the cathode and the contacting paste [20].

4 Modelling Approaches

The high operating temperature of SOFCs increases the costs of the experiments, the issues related to instrumentation implementation and hinder to draw unambiguous conclusions from post-test analyses. Another characteristic of the SOFC field is the difficulty to uncouple the problems in experiments while keeping the multiphysics nature of the problems. Modelling is of particular interest to overcome these difficulties.

4.1 Information Flow

Structural issues at the SRU scale are commonly investigated by importing the temperature and/or the vacancy profile generated by a thermo-electrochemical

model in structural analysis tool. The former uses either the finite-volume, difference method or FEM, whereas the latter are based on the FEM. The effect of stress or partial mechanical failures on the electrochemical performance is not implemented at present. Depending on the issues to solve, the thermo-electrochemical model is dynamic and includes degradation processes. Dynamic mechanical effects are not included, because studies focus on stationary application. The full geometry must be included. Indeed, the consideration of a representative channel somewhat limits the relevance of the analysis, since critical mechanical failures can occur as well in introduction, exhaust and sealing zones. The locations of interest for gas flow distribution, electrochemical behaviour and mechanical stress differ, hence so do the meshes. Here, the simplest and quickest strategy, if applicable, for the importation of the profiles generated by the thermo-electrochemical models is to enable a layer-by-layer importation that spares the need for three-dimensional interpolation.

4.2 Choice of Elements and Contact Algorithm

The different components are meshed and their interaction modelled by the contact algorithm or constrain method of the software [1]. The contact pair tracking methods depend on the software. Except during the assembly of the cell, which can be simplified, the relative motion of the SRU components is small, since it is mostly driven by the differences in thermal and isothermal expansion. This enables the use of a simpler small-sliding tracking method, to reduce the computation time. Similarly, the correction for nonlinear geometric effects is not required in common situations, since large deformations are not expected.

The computation demand in contact simulation is high. Therefore, first order solid or continuum shell elements are favoured [1]. Most of the studies at the SRU scale do not include the effect of the curvature of the cell on the interaction with the other components. Here, at the cell scale, an approach is to use a combination of second-order solid elements for the supporting layer and shell elements for the electrodes or interlayers. In most cases, the electrodes only partially cover the electrolyte that exhibits the strongest and most durable adhesion with the sealing materials. Therefore, a dense mesh is required, which induces memory limitations with standard computing resources. Preliminary tests allow identifying and further restricting the details in the contact simulations to the layers that have the strongest influence on the curvature of the cell. The stress in the omitted layers can be investigated afterwards by using the submodelling capabilities of commercial software [1].

The simplest implementation of rate-independent plasticity and creep enforces, among others, the preservation of the volume. This might not describe the behaviour of GDL materials, such as metallic foams, and result in unrealistic predictions of loss of local contact, when coupled to a high friction coefficient. Depending on the technological solutions, special purpose elements for the modelling of gaskets that uncouple the transverse and through-the-thickness behaviour can serve for preliminary investigations [1].

4.3 Assessment of the Failure of Ceramic Materials

The knowledge of the stress field is a first step towards the analysis of the risks of failure of ceramic materials subjected to multiaxial stress, such as provided by the Weibull theory [122]. A postprocessing procedure based on the the principle of independent action (PIA) is straightforward to implement. In the case future studies highlight the limitations of this simplification, more refined theories exist, such as the Batdorf theory [57]. A complete analysis tool, CARES [94] is available.

4.4 Stacking

A specificity of the modelling of stresses in SOFCs is the stacking of the SRUs. The reduction of the thickness of the components, to decrease the thermal inertia, among others, promotes stacking issues: uneven distribution of the assembly load, increased effect of growing oxide scales, difficulties to ensure the reproducibility of the mechanical properties of some components, such as the GDL and sealants, or structural instabilities can cause contacting issues and direct or indirect cell failures. Few studies have been carried out on the overall deformation of a SRU embedded in a stack, because the number of SRUs that can be meshed is limited by the computation time in contact simulations [60, 63]. A complementary approach is to impose modified periodic boundary conditions on one SRU [88]. This is achieved by implementing linear multipoint constraints [88], which can be derived from those used for the modelling a unit cell in a cellular solid [31], depending on the design. In the classical case of a co- or counter-flow configuration, for instance, rotation around the y-axis (see Fig. 5) may not be prevented, which can be approximated by using help nodes. The simplest version of this approach is to enforce the flatness of the MIC [92].

4.5 Initialisation

The correct handling of the many manufacturing steps of an SOFC stack, i.e. (i) cell sintering, (ii) components assembly and stacking, (iii) sealing procedure and (iv) anode reduction, has a strong influence on the stress field in operation. The use of field variables to control the material properties already provides enough flexibility to handle most of the situations. Figure 6 depicts the different steps of the initialisation procedure.

The cell sintering phase can be simplified by setting artificial CTEs in the electrolyte, anode-compensating layer and cathode, to comply with the use of the small-sliding tracking method. The CTE of the anode equals to zero during this step. Thus, the sintering phase corresponds to an increase of 1 K of the cell [92]. The simpler possibility is to determine the values of the artificial CTEs corresponding to the mismatch strain based on the zero-stress temperature [6, 129, 130]. A better one is to
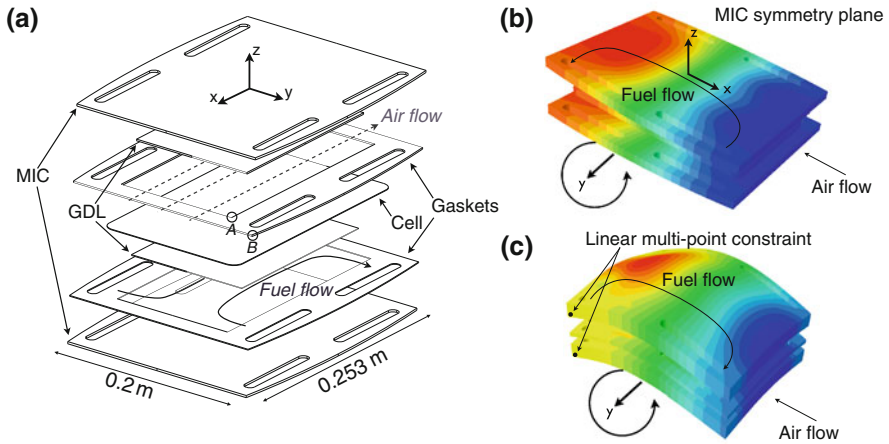
Fig. 5 Schematic view of **a** the Flame SOFC SRU design developed at LENI-EPFL [88, 92], reproduced here with kind permission from © Elsevier 2009 and different boundary conditions to model stacking conditions: **b** enforced flatness of the MIC, **c** modified periodic boundary conditions

Fig. 6 Description of the initialisation sequence for contact simulations, i layer of component, a anode, e electrolyte, c cathode, cp compensating layer, cl compatibility layer and k material [88]. Reproduced here with kind permission from © Elsevier 2012
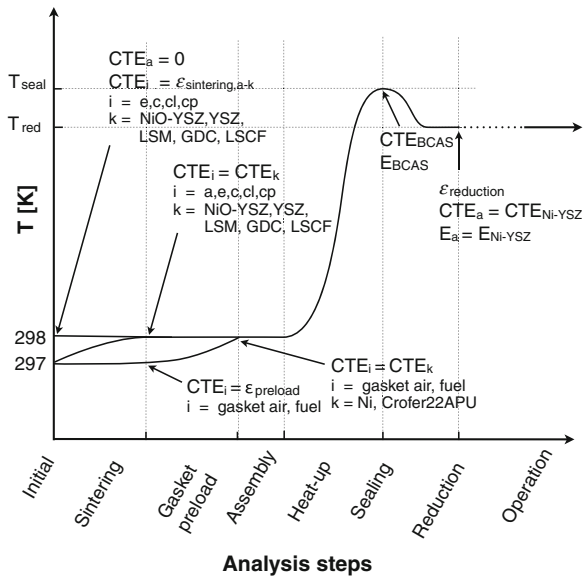
compute the irreversible strain generated during the cooldown after the sintering, depending on the cell materials and configuration and include it in the calculation of the artificial CTE [91]. The actual CTE are then reinserted in the model for the subsequent steps. The thickness of the gaskets before the assembly can differ from that of the GDL. This is a design variable, which can be used to control the distribution of the assembly pressure on the SRU. An additional initialisation step can be

added for this purpose, where an anisotropic and artificial thermal strain is induced prior to the assembly, in a similar manner to the sintering step.

In the case of a glass-ceramic sealant, the mechanical properties change after the sealing procedure. A possibility to approximate the progressive nature of the process is to first discretely modify the mechanical properties, then enable creep for the desired time period. In the case the emphasis is on the sealing system, the initialisation procedure can be simplified to an uniform value, which sets, in a first approximation, the reference state for the mechanical interaction with the other components [125]. If structural failure recurrently occurs during the sealing procedure, a more detailed analysis of the sealing procedure is possible with existing data, by combining calculations of the temperature profile to crystallisation kinetics [9], temperature-dependent viscosity [76], and temperature and composition dependent CTE [79] and Young's modulus [65].

The modification of the CTE and Young's modulus ensuing the anode reduction is straightforward to handle. In the simplified view allowed by the existing data, the shrinkage is uniform. It can be implemented either manually or using the swelling option available in most modelling tools. The temperature profiles generated by the thermo-electrochemical model can then be imported.

4.6 Interaction with Modelling at Smaller Scales

SOFC modelling, be it electrochemical or mechanical, is multiscale. The knowledge gained at the microscale must be implemented at the stack macroscale, through homogenisation techniques or combined homogenisation/localisation procedures, for instance. This is currently seldom achieved in thermo-electrochemical models [47] and almost never applied to mechanical aspects. Therefore, a quick overview of the modelling approaches at the smaller scale is worthwhile.

At the electrode scale, REV modelling of composite materials has been introduced recently in the SOFC field. It echoes that on electrochemical aspects, using the lattice Boltzmann method (LBM) [44, 108, 113]. The microstructure is either artificially generated [45, 67] or gathered from experiments [117], such as focused-ion beam-scanning electron microscope (FIB-SEM). Two different approaches exist, based on either the FEM method [45, 117] or discrete element method (DEM) [67]. The outcome is restricted at present to the prediction of the essential properties, such as CTE [45], the Young's modulus and strength [67], but the techniques have the capability to provide insights into the failure mechanisms.

At the component level, fracture mechanics is applied to study cracking in the glass-ceramic or at the sealing interfaces, commonly observed during thermal cycling. Finite fracture mechanics has been used to identify the critical locations in a glass-ceramic sealing system, in the light of a combined stress and energy criterion for the nucleation and subsequent propagation of cracks [85]. A set of discrete and continuum damage models have been applied to study cracking in the bulk of a ceramic-glass sealant, and at the interface between the glass-ceramic and a YSZ electrolyte [95].

5 Example of Applications and Results

The effective mitigation of mechanical failures requires combined actions at different scales:

- Improvement of the properties of the materials.
- Design of the cell.
- SRU and stack design.
- Stack operating strategy and system implementation.

The present chapter is not exhaustive. The emphasis is on the third and fourth point. The outcome of simple models, which can be applied for the second point, is included, since it can provide input values for contact analyses. In contrast, REV and fracture mechanics simulations, suited to address the first and second point, provide at present material properties or failure criteria. This situation is expected to change in a near future, since the implementation of the knowledge of the failure mechanisms at the stack scale, gained by refined experiments and dedicated models, will require integrated modelling approaches.

5.1 Models Based on the Euler–Bernoulli Theory

Simple models based on the Euler–Bernoulli theory, or on two-dimensional implementation in FEM tools, have many applications. They can provide an assessment of the sensitivity of stresses on the mechanical properties and configuration of the cell layers, and can efficiently estimate parameters from X-ray diffraction (XRD) stress measurements. The implementation of creep, shrinkage or expansion is straightforward, which enables prospective investigations of the reduction step, thermal and/or redox cycling and ageing conditions. Simple models can simplify the initialisation procedure in contact simulation (see Sect. 4.5), by determining the irreversible deformations generated during the cooldown after the sintering step, as a function of the cell materials and configurations, heating ramp and flattening process.

Zhang et al. [134] have computed the stress states, and ensuing probabilities of failure of the different layers in anode-supported cells, which enables an estimation of the required minimum thickness of the anode support, which withstands tensile stress. In their case, the benefit of a reduction of the tensile stress exceeds the detrimental increase in volume.

Liu et al. [64] have proposed failure criteria for different cracking scenario, such as cracks perpendicular to the interface in the cathode and edge cracks at the interfaces either between the anode and the electrolyte or between the electrolyte and the cathode. They illustrate how their approach can determine the maximum allowable curvature and warpage to withstand stack assembly, i.e. avoid cracking in the cathode and edge cracking at the electrolyte interfaces in the anode-supported

Fig. 7 Anode or electrolyte thickness effects on the number of thermal cycles until failure [62]. Reproduced here with kind permission from © Elsevier 2010
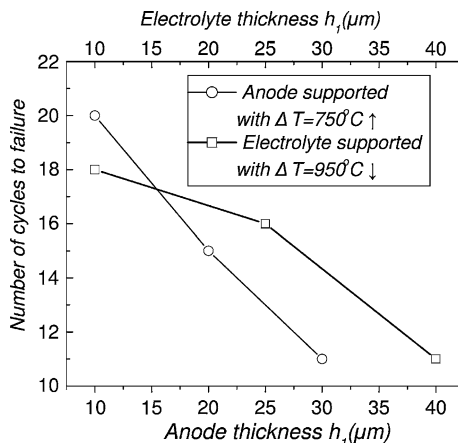

cell configuration. This is a criterion for a simple quality control procedure. In a next step [62], an approach has been developed to provide lifetime predictions during thermal cycling, based on the Paris law for crack nucleation and calculation of the peeling and shear stresses at the interface between the support and electrode, which are more concentrated near the cell edges. In their calculations, which focus on the anode/electrolyte interface in either anode-supported or electrolyte-supported cells, the porosity has overall a detrimental effect on the resistance against cycling, because it influences the initial damage distribution. The increase of the thickness of the thinner layer, that is electrolyte and anode, in anode-supported, respectively electrolyte-supported cells, reduces the number of cycles to failure, as shown in Fig. 7.

Subtle changes in the temperature dependence of the properties, can completely modify the failure modes. In anode-supported cells, models predict that the stress state in a LSM-based cathode can change from tensile to compressive, depending on the temperature [91]. Delamination of the cathode is experimentally observed and may arise from the compressive stress, through buckling, but the approaches developed in the field of TBC do not capture realistically the failure mode. In contrast, an LSCF cathode is always subjected to tensile stress and may crack [70]. Shielding compressive stress develops in the thin YSZ electrolyte, due to the lower CTE than the anode support. The same applies to the GDC or YDC compatibility layer, initially. The situation drastically changes during thermal cycles, after ageing at SOFC operating temperature, during 500–800 h due to the relief of the compressive stress and higher CTE of GDC or YDC, compared with that of the reduced anode, as shown in Fig. 8. Of course, the material properties govern the change in stress state and time scale of the phenomena.

The aforementioned results hold for the bulk of the materials. The stress field differs at the edges. Laurencin et al. [57] (see Fig. 9) have investigated the failure due to the singular stress field at the interfacial edges between the layers in anode and electrolyte-supported cells, under different conditions. The k-dominance radius

Fig. 8 Evolution of the stress in the different layers of an anode-supported cell with LSM cathode (*top*, 5LSM) and LSCF cathode (*bottom* 5LSCF), from the assembly, followed by the reduction step, and combined ageing at 1073 K and full thermal cycles (*l* left hand side axis, *r* right, *cl* compatibility layer, 5LSM 500 μm Ni-YSZ, 7μm YSZ, 60 μm LSM, 5LSCF 500 μm Ni-YSZ, 7 μm YSZ, 7 μm GDC, 60 μm LSCF) [91]. Reproduced here with kind permission from © John Wiley and Sons 2011
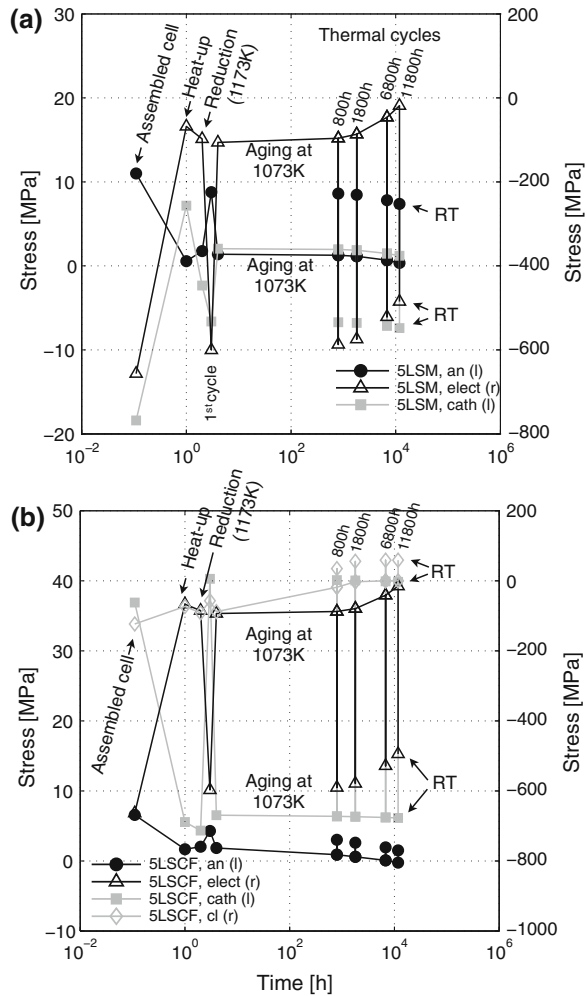
R_k is of 2 μm (anode-supported cell) and 6 μm (electrolyte-supported cell) at the electrolyte–cathode interface. This sets the limit of validity for a Weibull analysis applied on the whole cell. In anode-supported cell, the singularity at the anode/electrolyte interfacial edge does not govern the probability of failure of the anode and electrolyte. The singularity at the interface between the cathode and electrolyte is potentially detrimental for the latter, during redox cycling. In the case of residual stress at room temperature, the radius of the exclusion zone is of 0.5 μm, which practically scales with the size of the particles. Because an electrolyte-supported cell is almost symmetric, the effect of the singularity is identical at the interfaces between the electrolyte and anode or cathode. It does not affect the electrodes, but may initiate the cracking of the electrolyte from defects located in a zone of approximately 6 μm.
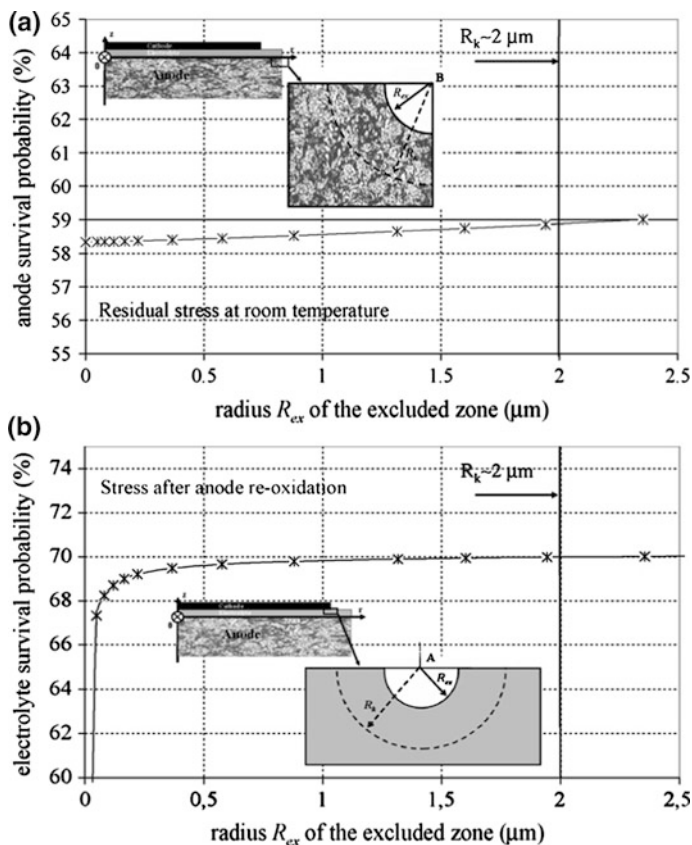
Fig. 9 **a** Survival probability of the anode substrate calculated by removing from the domain of integration a region surrounding the singularity B (case of the residual stress at room temperature). **b** Survival probability of the electrolyte substrate calculated by removing from the domain of integration a region surrounding the singularity A (case of the stress after anode re-oxidation with a bulk expansion of $\epsilon_{ox} = 0.14\%$ and an uncracked cathode) [58]. Reproduced here with kind permission from © Elsevier 2007

The study by Sato et al. [105] has shown that isothermal expansion likely governs the failure of electrolyte-supported cells, based on $Ce_{0.8}Sm_{0}.2O_{2-\delta}$ above 973 K. This is in accordance with other studies on the topic [5].

Malzbender et al. [74] have studied the influence of the cell curvature on the residual stresses before and after the reduction of the anode, yielding an estimation of the reduction strain in the range of 0.1 %. Their model has also been used to examine the oxidation–reoxidation of the anode support [75]. In the case of a thin anode support of 0.27 mm, a model with the anode functional layer of lower porosity provided a better prevision of the evolution of the curvature during reoxidation. Sun et al. [112] have derived values from the analysis of the curvature of the anode support. The behaviour differs, depending on the anode support arrangement, i.e.

presence or not of a compatibility layer. Sun et al. [112] hence suggest that a significant amount of plastic deformation of the Ni phase occurs during reduction.

XRD measurements exhibit a nonlinear relation between the stress and temperature in the electrolyte in anode-supported cells [29, 71, 129, 130]. The variation of the stress that ensues the reduction of the support is smaller than expected, which shows that the shrinkage of the anode support compensates the decrease in Young's modulus. Lara Curzio et al. [56] have monitored the evolution of the stress in the electrolyte during ageing and thermal cycling. As expected, the magnitude of the compressive stress in the electrolyte first decreased at the beginning of both ageing and cycling, but then unexpectedly increased again. The former trend has been attributed to creep, while further work is required to relate the latter to the observed slight coarsening of small Ni grains. Different zero-stress temperatures lead to very strong variations in the computed stress in the electrolyte. The aforementioned trends could be qualitatively reproduced by implementing creep in a simple mode based on the Euler–Bernoulli beam theory, rather than adjusting the zero-stress temperature [91]. The compressive stress in the electrolyte ranges from 700 MPa to less than 50 MPa, depending on the cell geometry, temperature and state of the anode. The irreversible strain is positive (elongation) in the anode and negative (shrinkage) in the electrolyte and compensating layer, and small in the cathode. In the compatibility layer, it depends on the presence or not of a compatibility layer. More refined approaches have been used to improve the sintering process of the support [19].

Liu et al. [66] estimated the lifetime of the MIC before spallation of the oxide scales, and showed that a protective coating can delay the occurrence of spallation by a factor of 3, by slowing the growth of the oxide scale.

5.2 Focus on Single Stack Components

The SRU components can cause the loss of integrity of the cell, directly through mechanical interaction, or indirectly, because of the sequence of deleterious effects activated by its failure. A local loss of gas tightness detrimentally exposes the materials of the cathode (anode) compartment to reducing (oxidising) gases. Unsteady parasitic combustions provoke hot spots [25, 128]. The difficulty to ensure the reproducibility of the mechanical properties of the sealants and GDL materials [8, 110] is a cause of uneven gas supply among the stacked SRUs, of altered electrical contact and of partial loss of contact pressure on compressive gaskets.

At the SRU scale, the sealing solution has received most of the attention. The studies by Weil at al. [124, 125], Jiang et al. [43] and Lin et al. [61] compare the BCS, glass-ceramics and compressive gaskets. The former induce a less stringent joining than glass-ceramic during thermal cycles and partially alleviate the mismatch between the thermal expansions of the parts, while providing a better sealing performance than compressive gaskets. The cell to foil material, typically made of
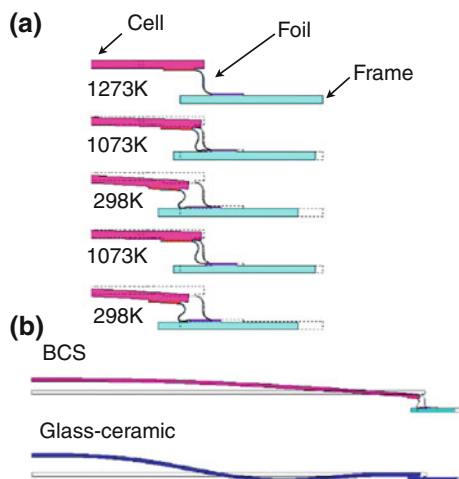
Fig. 10 a A series of cross-sectional images based from FE analysis depicting how the BCS components change in size and shape at the corner of the seal as a function of cooling from the stress-free state at 1273 K to room temperature and upon re-heating to 1073 K and cooling back to room temperature. The original size/shape of the components at the stress-free state are denoted by the dotted lines. **b** Schematics of cell deflection for the BCS and glass-ceramic seal designs: cross-sectional view along the diagonal of the cell [125]. Reproduced here with kind permission from © Elsevier 2008

silver braze, undergoes plastic deformation that relieves the stress in the cell [124]. The resulting history-dependence is moderate, as shown in Fig. 10 . The BCS results in a reduction of the stress and deflection compared with the glass-ceramic solution, which lets anticipate less contacting issues with the GDL. Therefore, an increase in foil thickness increases the stress in the cell in the range of 5–10 %. This must be balanced with oxidation issues for the long-term use [132]. The study by Jiang et al. [43] shows that the contribution of the temperature profile, neglecting the residual stress due to the multilayer nature of the cell, modifies the stress in the cell in the range of 30–40 %, approximately. The stress in the cell scales with the voltage, because the higher polarisation losses induce an increase of the temperature, hence decrease of the temperature difference with the reference state. The results of Govindaraju et al. [35] suggest that extreme care is required during the transient operation of a stack with glass-ceramic sealants. The relaxation of the stress in the cell occurs predominantly during less than 1 h after a discrete and significant change in applied temperature profile.

Yakabe et al. [131] have computed large stresses reaching 20–100 MPa in LaCrO$_3$ interconnects. The non-uniform isothermal expansion contributes to 8–80 % of the stress depending on the material and operating conditions. Therefore, the distribution of the vacancy profile and the dependence of the isothermal strain are crucial in the selection of the operating conditions and materials to avoid interconnect cracking, and indirectly, through mechanical interaction, cell failure. MIC are not prone to such issues but the uneven temperature profile can cause its buckling.

The shape of the temperature profile dictates the minimum stable thickness. Typical values range from 1–1.8 mm for a MIC of 400 cm^2 in typical operating conditions, and cannot be reliably predicted from simple indicators, such as the temperature difference over the SRU or maximum thermal gradient [93]. The occurrence of thermal buckling can be acceptable if it does not provoke large displacements or plastic deformation. The predicted remaining deflection of a free buckled MIC exhibiting a purely elastic behaviour can reach 3.5 mm, which is a likely source of loss of electrical contact and gas tightness, and modification of the stress in the cell. The results show that this phenomenon precludes any unconsidered decrease of the thickness of the MIC.

Selimovic et al. [107] have investigated the stress in a free single planar cell, subjected to steady-state and transient temperature profiles. The use of either ceramic or metallic interconnects affects the magnitude of the stress, due to the different thermal conductivities.

5.3 Stress Analyses of Stacks

Thermo-electrochemical optimisation is commonly performed at the system level. At the SRU scale, reliability and durability, rather than best initial performance are the main issues to solve. The modelling tools reliably predict the performance, but do not include the multiple possible origins of failures, which is needed to correctly discriminate the candidate designs at the early stage of the development of a stack. Currently, structural analyses of stack and SRU are prospective since they seek to identify the possible issues that may arise during operation. Their reliability has not yet been proven and to our knowledge, calibration is lacking. Studies focusing on button-cell tests with the framework described in Sect. 4 have been published, with the probable intention to further validate the models [15, 16, 58]. The simulations by Chiang et al. [16] show that stress in the cell scales inversely with operating voltage, because of the higher temperature difference, and suggest to keep thermal gradients lower than 10.6 K mm^{-1}. In contrast, the applied assembly load, from 0.5 to 1.0 kg cm^{-2} has a minor effect.

Lin et al. [60, 61] have meshed a planar, intermediate-temperature three-cell stack based on anode supported-cells and a glass-ceramic sealant, with linear continuum shell elements (see Fig. 11). The maximum principal stress in the PEN reaches 170 MPa at room temperature and decreases to 70 MPa in operation, because of the smaller temperature difference with the reference state. The MIC undergoes significant plastic deformation. In operation, the elastic modulus of the glass-ceramic sealant has been reduced by two thirds for a first assessment of the effects of the viscous behaviour. It results in a decrease of the stress of 10 % in the cell. Few studies have been carried out on the overall deformation of a SRU embedded in a functional stack. In the conditions of their simulations, a limited influence of the stack support conditions and position in the stack on the stress profile has been highlighted (see Fig. 11).

Fig. 11 a Schematic of the finite element model for one-half of a three-cell SOFC stack [61]. **b** Distribution of maximum in-plane principal stress in the MEA at steady operation for the *top*, *middle*, and *bottom* cells [60]. Reproduced here with kind permission from © Elsevier 2007, 2009
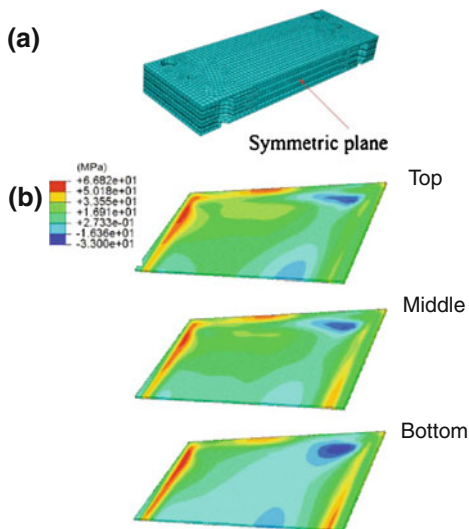
In Refs [88, 89, 92, 93], a thermo-electrochemical model, which includes degradation phenomena has been coupled with a structural analysis tool to study the mechanical reliability and durability of intermediate temperature, anode-supported SOFC stacks. This has allowed to provide insights into compromises between the requirements from thermo-electrochemical and mechanical aspects. The latter were analysed in the light of cell failure, provided by Weibull analysis, possible loss of electrical contact and gas-tightness, tentatively assessed from the distribution of the contact pressure and maximum tensile stress in the glass-ceramic sealant. Depending on the mechanical properties of the materials, the anode, solely, or together with the cathode, contribute to the cell probability of failure. The specificities of the temperature distribution and the level of mechanical interaction between the SRU components govern the risks of failure, which is illustrated in Figures 12 and 13. The properties of the GDLs, the thickness of the MIC and the deflection of the SRU, due to the cell residual stress and temperature profile, have in comparison a small impact on the cell probability of failure. Figure 14 shows that the anode and the cathode exhibit opposite dependences on operating conditions. The shape of the temperature profile affects the stress in the anode, whereas the stress state in the LSM–YSZ cathode is either tensile or compressive, depending on the thermal mismatch strain with the other layers at a given temperature. Therefore, stress increases in the anode, respectively decreases in the cathode, during current-voltage characterisation as current is drawn from the stack.

Cell mechanical reliability places different constraints on the operating conditions than thermo-electrochemical degradation, as shown in Fig. 13 by the probability of failure approximately one order of magnitude higher at $0.2\,\mathrm{W\,cm^{-2}}$, than at $0.3\,\mathrm{W\,cm^{-2}}$. The analysis performed in [92] reveals that transient operation
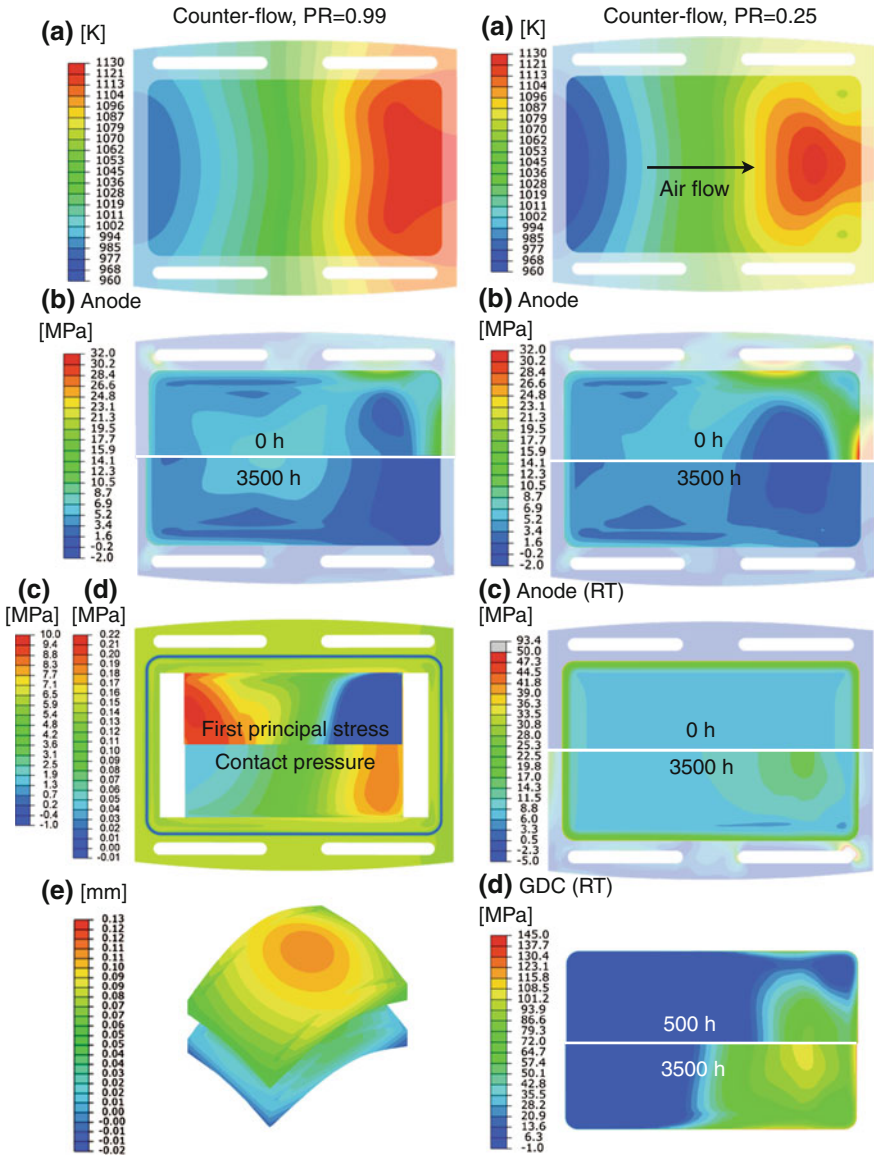
Fig. 12 *Left* Effect of the flow configuration and methane conversion fraction (PR) on the stress. Case of an anode-supported cell with LSM-YSZ cathode and compressive gaskets. **a** Temperature profile and **b** First principal stress in the anode. The MIC is displayed in transparency. **c** First principal stress in the cathode (insert above the symmetry line). **d** Contact pressure on the cathode GDL and compressive gasket and **e** vertical displacement along the z-axis, with an amplification factor of 2,000. *Right column* effect of creep in a cell based on a LSCF cathode and **a** temperature distribution, on **b** the evolution of the first principal stress in the anode support in operation and **c** during thermal cycling to RT and **d** evolution of the first principal stress in the GDC compatibility layer after thermal cycling. The profiles above and below the symmetry axis refer to different operation time [88, 89]. Reproduced here with kind permission from © Elsevier 2012

Fig. 13 Comparison of the anode and cathode probabilities of failure for the GSK (compressive gaskets), GSKT (compressive gaskets tied at the sealing interfaces) cases and enforced flatness of the MICs in the co-flow (PR = 0.99 %) and counter-flow (PR = 0.25 % or PR = 0.99 %) configuration. The system specific power is 0.21, 0.25 or 0.29 W cm^{-2} and the MIC thickness is 2 mm. Inserted values refer to the anode probability of failure at 0.29 W cm^{-2} [86]. Reproduced here with kind permission from © Elsevier 2012. The considered SRU geometry is depicted in Fig. 5
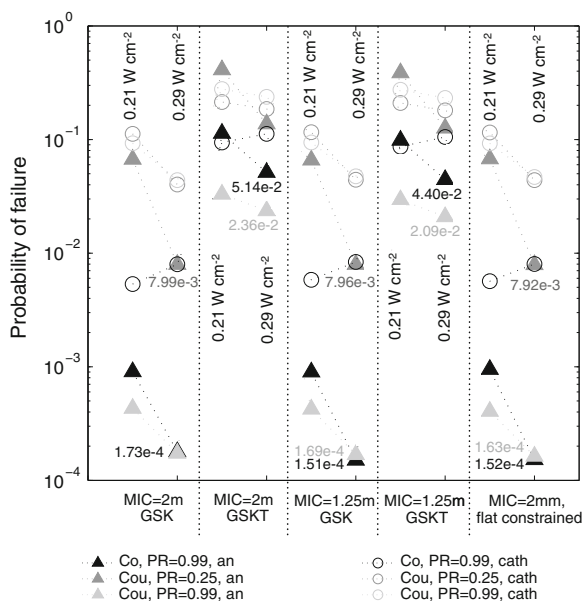
potentially generates the most critical conditions, if the control strategy is defective. Here, spatial temperature control is of interest to alleviate mechanical failure during load following [26]. The drastic decrease of the cell probability of failure during 10 h of annealing, in the case of a glass-ceramic sealant, suggests a possible vulnerability of this sealing solution to load following conditions. This altogether shows that simple relations between probability of failure and cell potential or current density do not reflect practical conditions. Similarly, maximum temperature difference and thermal gradients are imperfect indicators for cell cracking probability. For a given value, the probability of failure covers more than two orders of magnitude, as depicted in Fig. 15. This invalidates their use for design purposes and care is needed for control purposes. Furthermore, the uncertainty in the Weibull parameters for SOFC materials available in literature affects the calculation of the cell probability of failure by one to two orders of magnitude, at least [92].

Figure 16 shows that the contact pressure on the sealing gaskets depends on history and location. Controlled preload and/or consolidation steps are needed to ensure an acceptable level of gas-tightness in all zones during operation. The current knowledge on the mechanical properties of the GDLs and on the nature of the interactions at the interfaces does not allow a reliable and comprehensive assessment of possible losses of electrical contact. The temperature profile governs the distribution of the contact pressure on the GDL, which can however be controlled by adjusting the compliance of adjacent components and levels of mechanical interaction at the sealing interfaces. Therefore, in the case of a glass-ceramic sealant, the thermal mismatch strains, rather than the assembly load, govern the magnitude of the compressive stress on the GDL. Significantly higher
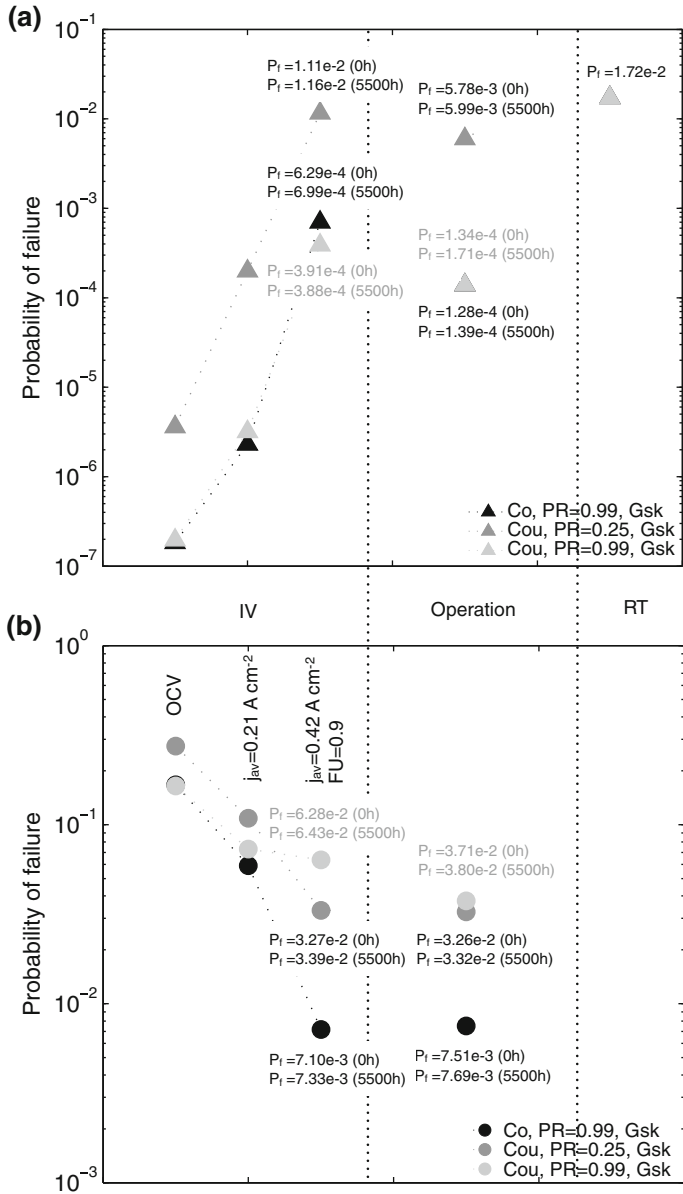
Fig. 14 Evolution of **a** the anode and **b** cathode probability of failure during IV characterisation, operation at the nominal point with creep of the GDL and MIC and thermal cycle to room temperature for the co- (CO) and counter-flow (COU) configuration [89]. Anode-supported cell and compressive gaskets and SRU geometry depicted in Fig. 5. *PR* methane conversion fraction in the reformer, *j* current density, *FU* fuel utilisation, P_f probability of failure. Reproduced here with kind permission from © Elsevier 2012

Fig. 15 Correlation between probability of failure and temperature difference (**a**) and thermal gradients (**b**) over the SRU [92]. TPOX thermal partial oxidation, SMR internal steam-methane reforming. Reproduced here with kind permission from © Elsevier 2009
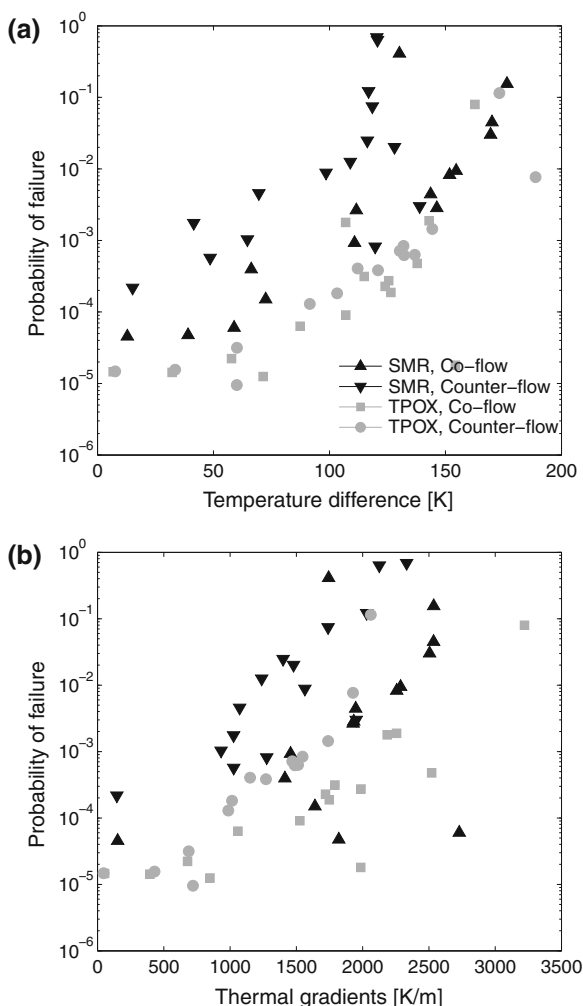
values than anticipated by the assembly load, approximately twice higher in the situation treated in [88], can arise and further generate an enhanced sensitivity to cycling conditions because of irreversible deformation in the GDL.

The modification of the temperature profile due to degradation, and creep in the MIC and GDLs, have a limited impact on the probability of failure of the cell. The latter typically increases by 10–50 % during IV characterisation, after 4,500 h of operation (see Fig. 14), which remains small compared to the variations induced by the operating conditions or choice of a sealing solution (i.e. in the range of one to two orders of magnitude). In contrast, creep in the components governs the evolution of the contact pressure on the GDL. During constant operating conditions, it flattens the contact pressure distribution (see Fig. 17). The generated

Fig. 16 Details of the evolution of the pressure versus closure in a compressive gasket. Anode-supported cell without anode compensating layer, hermal partial oxidation reformate and counter-flow configuration. Locations A and B refer to Fig. 5. Assembly and heat-up (*grey crosses*), current-voltage characterization (*black squares*), variation of the electrical load (*grey triangles*) and load shutdown and cooldown (*black stars*) [93]. Reproduced here with kind permission from © Elsevier 2009
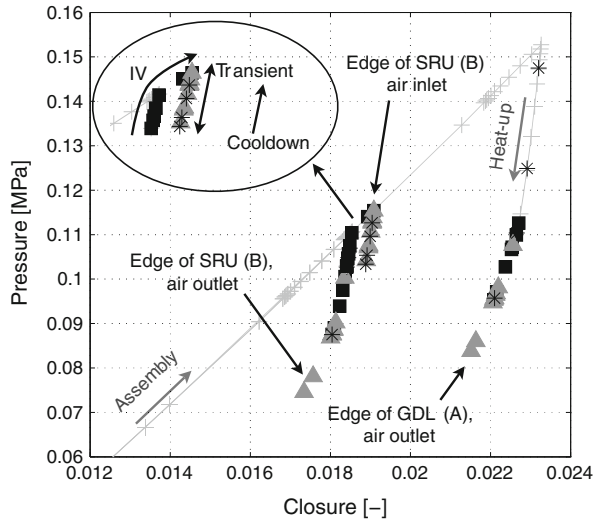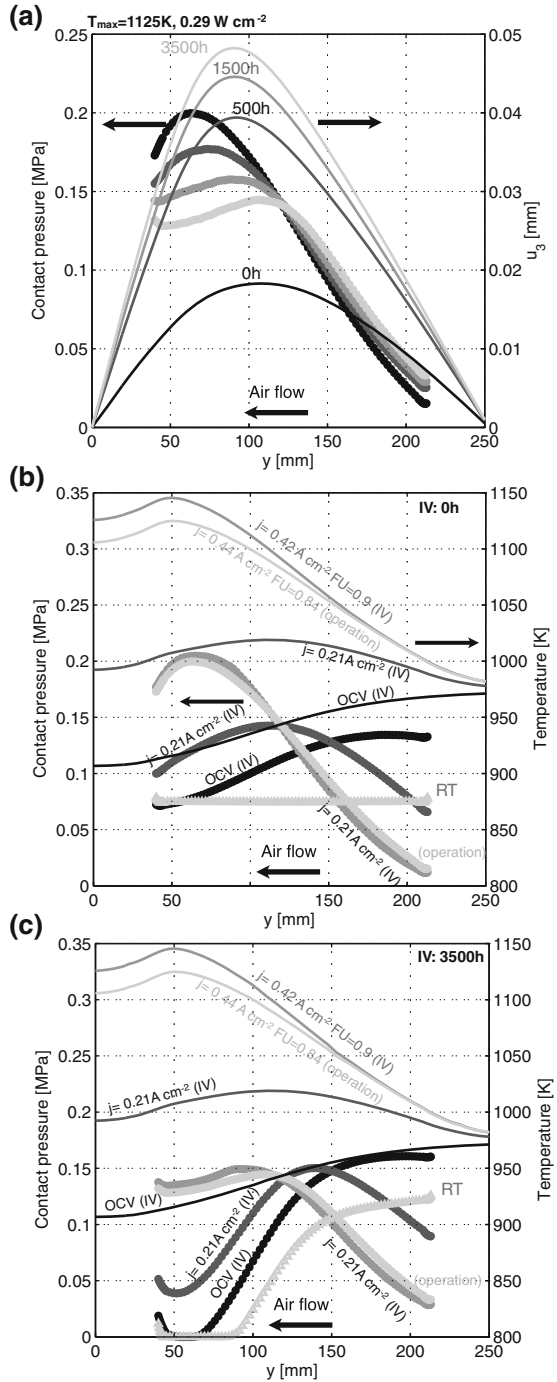
non-uniform irreversible deformation, combined to the increase of the SRU deflection, then induces a complete release of the compressive stress during IV characterisation and thermal cycling, in the zone subjected to the highest temperature during constant operation, as shown in Fig. 17. Practically, the contact pressure is lost over approximately half of the active area during thermal cycling. Further experiments and model improvements are needed to relate these results with a possible alteration of the electrical contact.

In a cell with LSCF cathode, tensile stress develops in the GDC compatibility layer during thermal cycling. The creep strain rate in the MEA layers is not evenly distributed, due to the temperature profile and thermal stress in operation (see Fig. 12). This typically doubles the tensile stress at room temperature in the zone of highest temperature during operation. The stress, in the range of 100 MPa, likely induces cracking of the GDC layer.

The feedback of the structural model on the thermo-electrochemical model is not considered in the studies, but will receive growing interest. The first investigation of the effect of disparities in the creep behaviour of anode GDL materials is available in [90]. The correction of the anode gas flux proceeds by comparing the nominal situation with a worst case, respectively characterised by a nominal creep strain rate and a twice higher one. For a comprehensive analysis, the overall bending of a SRU in a stack and the creep behaviour of components adjacent to the GDL, as well as thermal coupling between SRUs unevenly supplied in fuel should be accounted for. Figure 18 shows that the degradation of a SRU embedded in a stack, due to a progressive undersupply in fuel, strongly depends on the operating conditions.
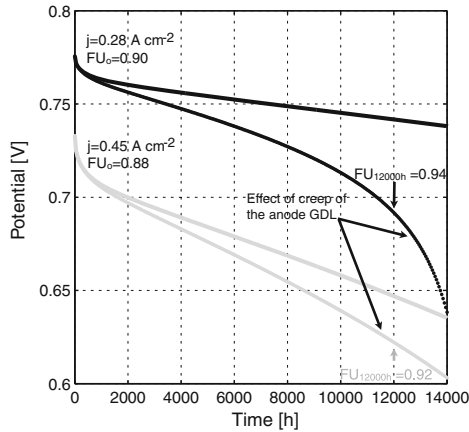
Fig. 18 Effect of fuel undersupply of a SRU in a stack due to creep in the anode GDL (*lines* no creep, *dots* with creep), during operation at a constant current density, corresponding to initial specific system power of 0.2 W cm^{-2} (*black*) and 0.3 W cm^{-2} (*grey*). Counter-flow configuration, 25 % of pre-reformed methane and maximum allowable temperature of 1150 K. j current density, *FU* fuel utilisation [90]. Reproduced here with kind permission from © Elsevier 2012

6 Future Work

Current SRU models can address several of the observed mechanical failures and highlight their strong sensitivity to subtle changes in the properties of the materials, of the interfaces, operating conditions and history. This qualitatively complies with the difficulties to mitigate in practice mechanical failures in SOFC stacks. The reliability of the prediction and exploitation of the modelling tools however suffer from the lack of knowledge on (i) the mechanical properties of all the materials, e.g. elastic, rate-independent plastic, creep behaviour and strength, (ii) the type of interactions between the components, (iii) effect of ageing or cycling, whereas (iv) experimental data dedicated for calibration is not available.

The potential for model improvements allowed by todays modelling capabilities is considerable, which lets anticipate significant improvements in the accuracy and variety of the simulated predictions. Once the failure mechanisms are understood, simplifications will be possible for the efficient implementation of both electrochemical and mechanical aspects in design models, in the view of both reliability and durability.

The particularity of mechanical issues in SOFC is their intricate link with the physico-chemical and electrochemical properties of the materials. Indeed, unlike for TBC or ceramic combustors, the main requirement for the ceramic materials is not their temperature and mechanical resistance, but electrochemical properties. Therefore, to go further towards reliable lifetime predictions, hence effective mitigation of mechanical failure, the multiphysics nature of the problem must be fully acknowledged and not restricted to thermal, or isothermal stress. Dedicated experiments combined to REV simulations can provide insights into the complex failure

modes that affect the composite ceramic materials, in view of the morphological and compositional alterations that result from prolonged use. Multi-scale modelling approaches must be used to integrate the outcome at the stack level. The growing interest in such techniques is encouraging. Similarly, the procedures to tackle efficiently stacking issues, in regard of dimensional tolerances, with a feedback on the thermo-electrochemical calculations, must be developed.

The literature does not comprise many experimental data to test first the relevance of the assumptions, and then calibrate the models. Despite the importance of confidentiality issues in electrode and stack engineering, massive efforts on such tasks are needed to propose general modelling frameworks.

Thermo-electrochemical performance or degradation considerations can be included in optimisation problems fairly easily. They entail trade-offs, which must be further completed by mechanical aspects. This knowledge will provide comprehensive guidance in design and synthesis of control.

References

1. ABAQUS Inc., v6.8, Hibbitt, Karlsson and Sorensen, Rhode Island
2. J. Adams, Young's modulus, flexural strength, and fracture of yttria-stabilized zirconia versus temperature. J. Am. Ceram. Soc. **80**(4), 903–908 (2000)
3. C. Appel, N. Bonanos, A. Horsewell, S. Linderoth, Ageing behaviour of zirconia stabilised by yttria and manganese oxide. J. Mater. Sci. **36**(18), 4493–4501 (2001)
4. M. Ashby, H. Frost, *Deformation Mechanism Maps: The Plasticity and Creep of Metals and Ceramics* (Pergamon Press, Oxford, 1982)
5. A. Atkinson, Chemically-induced stresses in gadolinium-doped ceria solid oxide fuel cell electrolytes. Solid State Ionics **95**(3–4), 249–258 (1997)
6. A. Atkinson, A. Selçuk, Residual stress and fracture of laminated ceramic membranes. Acta Materialia **47**(3), 867–874 (1999)
7. A. Atkinson, A. Selçuk, Mechanical behaviour of ceramic oxygen ion-conducting membranes. Solid State Ionics **134**(1–2), 59–66 (2000)
8. X. Badiche, S. Forest, T. Guibert, Y. Bienvenu, J.D. Bartout, P. Ienny, M. Croset, H. Bernet, Mechanical properties and non-homogeneous deformation of open-cell nickel foams: application of the mechanics of cellular solids and of porous materials. Mater. Sci. Eng. A **289**(1–2), 276–288 (2000)
9. N.P. Bansal, E.A. Gamble, Crystallization kinetics of a solid oxide fuel cell seal glass by differential thermal analysis. J. Power Sources **147**(1–2), 107–115 (2005)
10. P. Batfalsky, V. Haanappel, J. Malzbender, N. Menzler, V. Shemet, I. Vinke, R. Steinbrech, Chemical interaction between glass-ceramic sealants and interconnect steels in SOFC stacks. J. Power Sources **155**(2), 128–137 (2006)
11. S. Biswas, T. Nithyanantham, N. Saraswathi, S. Bandopadhyay, Evaluation of elastic properties of reduced NiO-8YSZ anode-supported bi-layer SOFC structures at elevated temperatures in ambient air and reducing environments. J. Mater. Sci. **44**(3), 778–785 (2009)
12. A. Bouzid, H. Champliaud, Contact stress evaluation of nonlinear gaskets using dual kriging interpolation. J. Press. Vessel Technol. **126**(4), 445–450 (2004)
13. M. Bram, S. Reckers, P. Drinovac, J. Mönch, R.W. Steinbrech, H.P. Buchkremer, D. Stöver, Deformation behavior and leakage tests of alternate sealing materials for SOFC stacks. J. Power Sources **138**(1–2), 111–119 (2004)

14. H.-T. Chang, C.-K. Lin, C.-K. Liu, High-temperature mechanical properties of a glass sealant for solid oxide fuel cell. J. Power Sources **189**(2), 1093–1099 (2009)

15. L.-K. Chiang, H.-C. Liu, Y.-H. Shiu, C.-H. Lee, R.-Y. Lee, Thermo-electrochemical and thermal stress analysis for an anode-supported sofc cell. Renew. Energy **33**(12), 2580–2588 (2008)

16. L.-K. Chiang, H.-C. Liu, Y.-H. Shiu, C.-H. Lee, R.-Y. Lee, Thermal stress and thermo-electrochemical analysis of a planar anode-supported solid oxide fuel cell: effects of anode porosity. J. Power Sources **195**(7), 1895–1904 (2010)

17. Y.-S. Chou, J.W. Stevenson, P. Singh, Effect of aluminizing of Cr-containing ferritic alloys on the seal strength of a novel high-temperature solid oxide fuel cell sealing glass. J. Power Sources **185**(2), 1001–1008 (2008)

18. C.-L. Chu, J.-Y. Wang, S. Lee, Effects of $La_{0.67}Sr_{0.33}MnO_3$ protective coating on SOFC interconnect by plasma-sputtering. Int. J. Hydrogen Energy **33**(10), 2536–2546 (2008)

19. M. Cologna, V.M Sglavo, Vertical sintering to measure the uniaxial viscosity of thin ceramic layers. Acta Materialia **58**(17), 5558–5564 (2010)

20. G. Delette, J. Laurencin, M. Dupeux, J. Doyer, Measurement of the fracture energy at the interface between porous cathode layer and electrolyte in planar solid oxide fuel cells. Scripta Materialia **59**(1), 31–34 (2008)

21. S. Diethelm, J. Van herle, Z. Wuillemin, A. Nakajo, N. Autissier, M. Molinelli, Impact of materials and design on solid oxide fuel cell stack operation. J. Fuel Cell Sci. Technol. **5**(3), 3–6 (2008)

22. C. D'Souza, N. Sammes, Mechanical properties of strontium-doped lanthanum manganite. J. Am. Ceram. Soc. **83**(1), 47–52 (2000)

23. A. Evans, J. Hutchinson, The thermomechanical integrity of thin films and multilayers. Acta Metallurgica et Materialia **43**(7), 2507–2530 (1995)

24. A.G. Evans, D.R. Mumm, J.W. Hutchinson, G.H. Meier, F.S Pettit, Mechanisms controlling the durability of thermal barrier coatings. Prog. Mater. Sci. **46**(5), 505–553 (2001)

25. A. Faes, A. Nakajo, A. Hessler-Wyser, D. Dubois, A. Brisse, S. Modena, J. Van herle, Redox study of anode-supported solid oxide fuel cell. J. Power Sources **193**(1), 55–64 (2009)

26. M. Fardadi, F. Mueller, F. Jabbari, Feedback control of solid oxide fuel cell spatial temperature variation. J. Power Sources **195**(13), 4222–4233 (2010)

27. J.W Fergus, Metallic interconnects for solid oxide fuel cells. Mater. Sci. Eng. A **397**(1–2), 271–283 (2005)

28. J.W Fergus, Sealants for solid oxide fuel cells. J. Power Sources **147**(1–2), 46–57 (2005)

29. W. Fischer, J. Malzbender, G. Blass, R. Steinbrech, Residual stresses in planar solid oxide fuel cells. J. Power Sources **150**, 73–77 (2005)

30. A.S for Testing and Materials. Standard Test Method for Monotonic Equibiaxial Flexural Strength of Advanced Ceramics at Ambient Temperature. ASTM standard C1499-04

31. M. Galli, J. Botsis, J. Janczak-Rusch, An elastoplastic three-dimensional homogenization model for particle reinforced composites. Comput. Mater. Sci. **41**, 312–321 (2008)

32. L. Gibson, M. Ashby, *Cellular Solids: Structure and Properties* (Cambridge University Press, Cambridge, 1999)

33. S. Giraud, J. Canel, Young's modulus of some SOFCs materials as a function of temperature. J. Eur. Ceram. Soc. **28**(1), 77–83 (2008)

34. R. Goodall, C. Williams, J. Fernie, T. Clyne, et al., Thermal expansion and stiffness characteristics of a highly porous, fire-resistant composite material, in *International SAMPE Symposium and Exhibition (Proceedings)*, vol. 47, pp. 1001–1010

35. N. Govindaraju, W. Liu, X. Sun, P. Singh, R. Singh, A modeling study on the thermomechanical behavior of glass-ceramic and self-healing glass seals at elevated temperatures. J. Power Sources **190**(2), 476–484 (2009)

36. L. Grahl-Madsen, P. Larsen, N. Bonanos, J. Engell, S. Linderoth, Mechanical strength and electrical conductivity of Ni-YSZ cermets fabricated by viscous processing. J. Mater. Sci. **41**(4), 1097–1107 (2006)

37. F. Gutierrez-Mora, J.M. Ralph, J.L Routbort, High-temperature mechanical properties of anode-supported bilayers. Solid State Ionics **149**(3–4), 177–184 (2002)
38. C. Haering, A. Roosen, H. Schichl, Degradation of the electrical conductivity in stabilised zirconia systems: Part I: yttria-stabilised zirconia. Solid State Ionics **176**(3–4), 253–259 (2005)
39. J.S. Hardy, J.Y. Kim, E.C. Thomsen, K.S Weil, Improved wetting of mixed ionic/electronic conductors used in electrochemical devices with ternary air braze filler metals. J. Electrochem. Soc. **154**(3), 32–39 (2007)
40. T. Hashida, K. Sato, Y. Takeyama, T. Kawada, J. Mizusaki, Deformation and fracture characteristics of zirconia and ceria-based electrolytes for SOFCs under reducing atmospheres. ECS Trans. **25**(2), 1565–1572 (2009)
41. Haynes International. Material data sheet no. h-3000 h
42. F. Iguchi, Y. Endo, T. Ishida, T. Yokobori, H. Yugami, T. Otake, T. Kawada, J. Mizusaki, Oxygen partial pressure dependence of creep on yttria-doped ceria ceramics. Solid State Ionics **176**(5–6), 641–644 (2005)
43. T.L. Jiang, M.-H Chen, Thermal-stress analyses of an operating planar solid oxide fuel cell with the bonded compliant seal design. Int. J. Hydrogen Energy **34**(19), 8223–8234 (2009)
44. J. John R. Izzo, A.S. Joshi, K.N. Grew, W.K.S. Chiu, A. Tkachuk, S.H. Wang, W. Yun. Nondestructive reconstruction and analysis of SOFC Anodes using X-ray computed tomography at Sub-50 nm resolution. J. Electrochem. Soc. **155**(5), B504–B508 (2008)
45. J. Johnson, J. Qu, Effective modulus and coefficient of thermal expansion of Ni–YSZ porous cermets. J. Power Sources **181**(1), 85–92 (2008)
46. T. Kawada, S. Watanabe, S.ichi Hashimoto, T. Sakamoto, A. Unemoto, M. Kurumatani, K. Sato, F. Iguchi, K. Yashiro, K. Amezawa, K. Terada, M. Kubo, H. Yugami, T. Hashida, J. Mizusaki, Classification of mechanical failure in SOFC and strategy for evaluation of operational margin. ECS Trans. **25**(2), 467–472 (2009)
47. J. Kim, W. Liu, C. Lee, Multi-scale solid oxide fuel cell materials modeling. Comput. Mech. **44**(5), 683–703 (2009)
48. J.Y. Kim, J.S. Hardy, K.S Weil, Novel metal-ceramic joining for planar SOFCs. J. Electrochem. Soc. **152**(6), 52–58 (2005)
49. J. Kondoh, Aging strengthening of 8 mol% yttria-fully-stabilized zirconia. J. Alloys Compd. **370**(1–2), 285–290 (2004)
50. J. Kondoh, T. Kawashima, S. Kikuchi, Y. Tomii, Y. Ito, Effect of aging on yttria-stabilized zirconia. 1: a study of its electrochemical properties. J. Electrochem. Soc. **145**(5), 1527–1536 (1998)
51. J. Kondoh, S. Kikuchi, Y. Tomii, Y. Ito, Effect of aging on yttria-stabilized zirconia. J. Electrochem. Soc. **145**(5), 1550–1560 (1998)
52. J. Kondoh, S. Kikuchi, Y. Tomii, Y. Ito, Effect of aging on yttria-stabilized zirconia. 2: a study of the effect of the microstructures on conductivity. J. Electrochem. Soc. **145**(5), 1536–1550 (1998)
53. J. Kübler, R. Primas, B. Gut, Mechanical Strength of Thermally Aged and Cycled Thin Zirconia Sheets, Advances in Science and Technology, Ceramics: Charting the Future, ed. P. Vincenzini, Techna, Florence, Italy, ISBN 88-86538-02-2, 923–928 (1995)
54. B. Kuhn, F. Wetzel, J. Malzbender, R. Steinbrech, L. Singheiser, Mechanical performance of reactive-air-brazed (RAB) ceramic/metal joints for solid oxide fuel cells at ambient temperature. J. Power Sources **193**(1), 199–202 (2009)
55. A. Lakki, R. Herzog, M. Weller, H. Schubert, C.Reetz, O. Görke, M. Kilo, G. Borchardt, Mechanical loss, creep, diffusion and ionic conductivity of ZrO_2-8 mol% Y_2O_3 polycrystals. J. Eur. Ceram. Soc. **20**(3), 285–296 (2000)
56. E. Lara-Curzio, M. Radovic, M. Trejo, C. Cofer, T. Watkins, K. More, Effect of thermal cycling and thermal aging on the mechanical properties of, and residual stresses in, Ni-YSZ/YSZ bi-layers. IV.A.11 Reliability and durability of materials and components foe solid oxide fuel cells. Adv. Solid Oxide Fuel Cells II **27**(4), 383–391 (2007)

57. J. Laurencin, G. Delette, M. Dupeux, An estimation of ceramic fracture at singularities by a statistical approach. J. Eur. Ceram. Soc. **28**(1), 1–13 (2008)
58. J. Laurencin, G. Delette, F. Lefebvre-Joud, M. Dupeux, A numerical tool to estimate sofc mechanical degradation: case of the planar cell configuration. J. Eur. Ceram. Soc. **28**(9), 1857–1869 (2008)
59. H. Lein, K. Wiik, M. Einarsrud, T. Grande, E. Lara-curzio, High-temperature creep behavior of mixed conducting $La_{0.5}Sr_{0.5}FeCo_xO_{3-\delta}$ ($0.5 \leq x \leq 1$) materials. J. Am. Ceram. Soc. **89**(9):2895–2898 (2006)
60. C.-K. Lin, T.-T. Chen, Y.-P. Chyou, L.-K Chiang, Thermal stress analysis of a planar SOFC stack. J. Power Sources **164**(1), 238–251 (2007)
61. C.-K. Lin, L.-H. Huang, L.-K. Chiang, Y.-P Chyou, Thermal stress analysis of planar solid oxide fuel cell stacks: effects of sealing design. J. Power Sources **192**(2), 515–524 (2009)
62. L. Liu, G.-Y. Kim, A. Chandra, Modeling of thermal stresses and lifetime prediction of planar solid oxide fuel cell under thermal cycling conditions. J. Power Sources **195**(8), 2310–2318 (2010)
63. W. Liu, X. Sun, M. Khaleel, Effect of creep of ferritic interconnect on long-term performance of solid oxide fuel cell stacks. Fuel Cells **10**(4), 703–717 (2010)
64. W. Liu, X. Sun, M. Khaleel, J. Qu, Global failure criteria for positive/electrolyte/negative structure of planar solid oxide fuel cell. J. Power Sources **192**(2), 486–493 (2009)
65. W. Liu, X. Sun, M.A Khaleel, Predicting Young's modulus of glass/ceramic sealant for solid oxide fuel cell considering the combined effects of aging, micro-voids and self-healing. J. Power Sources **185**(2), 1193–1200 (2008)
66. W. Liu, X. Sun, E. Stephens, M. Khaleel, Life prediction of coated and uncoated metallic interconnect for solid oxide fuel cell applications. J. Power Sources **189**(2), 1044–1050 (2009)
67. X. Liu, C.L. Martin, G. Delette, D. Bouvard, Elasticity and strength of partially sintered ceramics. J. Mech. Phys. Solids **58**(6), 829–842 (2010)
68. Y. Liu, A. Hagen, R. Barfod, M. Chen, H. Wang, F. Poulsen, P. Hendriksen, Microstructural studies on degradation of interface between LSM-YSZ cathode and YSZ electrolyte in SOFCs. Solid State Ionics **180**(23–25), 1298–1304 (2009)
69. F. Lowrie, R. Rawlings, Room and high temperature failure mechanisms in solid oxide fuel cell electrolytes. J. Eur. Ceram. Soc. **20**(6), 751–760 (2000)
70. A. Mai, V.A. Haanappel, S. Uhlenbruck, F. Tietz, D. Stöver, Ferrite-based perovskites as cathode materials for anode-supported solid oxide fuel cells: Part I. Variation of composition. Solid State Ionics **176**(15–16), 1341–1350 (2005)
71. J. Malzbender, W. Fischer, R. Steinbrech, Studies of residual stresses in planar solid oxide fuel cells. J. Power Sources **182**(2), 594–598 (2008)
72. J. Malzbender, L. Singheiser, R. Steinbrech, A review of advanced techniques for characterising SOFC behaviour. Fuel Cells **9**(6), 785–793 (2009)
73. J. Malzbender, R. Steinbrech, L. Singheiser. Failure probability of solid oxide fuel cells, in *Ceramic Engineering and Science Proceedings*, vol. 26, pp. 293–298. American Ceramic Society, 2005
74. J. Malzbender, T. Wakui, R. Steinbrech, Curvature of planar solid oxide fuel cells during sealing and cooling of stacks. Fuel Cells **6**(2), 123–129 (2006)
75. J. Malzbender, E. Wessel, R. Steinbrech, Reduction and re-oxidation of anodes for solid oxide fuel cells. Solid State Ionics **176**(29–30), 2201–2203 (2005)
76. K. Meinhardt, D.-S. Kim, Y.-S. Chou, K. Weil, Synthesis and properties of a barium aluminosilicate solid oxide fuel cell glass-ceramic sealant. J. Power Sources **182**(1), 188–196 (2008)
77. D. Meixner, R. Cutler, Low-temperature plastic deformation of a perovskite ceramic material. Solid State Ionics **146**(3–4), 285–300 (2002)
78. N.H. Menzler, de L.G. Haart, D. Sebold, Characterization of cathode chromium incorporation during mid-term stack operation under various operational conditions. ECS Trans. **7**(1), 245–254 (2007)

79. J. Milhans, S. Ahzi, H. Garmestani, M. Khaleel, X. Sun, B. Koeppel, Modeling of the effective elastic and thermal properties of glass-ceramic solid oxide fuel cell seal materials. Mater. Des. **30**(5), 1667–1673 (2009)

80. A. Mitterdorfer, L.J. Gauckler, $La_2Zr_2O_7$ formation and oxygen reduction kinetics of the $La_{0.85}Sr_{0.15}Mn_yO_3$, $O_2(g)YSZ$ system. Solid State Ionics **111**(3–4), 185–218 (1998)

81. A. Morales-Rodriguez, A. Bravo-Leon, A. Dominguez-Rodriguez, S. Lopez-Esteban, J. Moya, M. Jimenez-Melendo, High-temperature mechanical properties of zirconia/nickel composites. J. Eur. Ceram. Soc. **23**(15), 2849–2856 (2003)

82. M. Mori, Effect of B-site doing on thermal cycle shrinkage for $La_{0.8}Sr_{0.2}Mn_{1-x}M_xO_{3+\delta}$ perovskites (M= Mg, Al, Ti, Mn, Fe, Co, Ni; $0 \leq x \leq 0.1$). Solid State Ionics **174**(1–4), 1–8 (2004)

83. M. Mori, Y. Hiei, N. Sammes, G. Tompsett, Thermal-expansion behaviors and mechanisms for Ca-or Sr-doped lanthanum manganite perovskites under oxidizing atmospheres. J. Electrochem. Soc. **147**, 1295 (2000)

84. M. Mori, T. Yamamoto, H. Itoh, H. Inaba, H. Tagawa, Thermal expansion of nickel–zirconia anodes in solid oxide fuel cells during fabrication and operation. J. Electrochem. Soc. **145**, 1374 (1998)

85. A. Müller, W. Becker, D. Stolten, J. Hohe, A hybrid method to assess interface debonding by finite fracture mechanics. Eng. Fract. Mech. **73**(8), 994–1008 (2006)

86. A. Nakajo, Thermomechanical and electrochemical degradation in anode-supported solid oxide fuel cell stacks. Ph.D Thesis, 4930, Ecole Polytechnique Fédérale de Lausanne, 2011

87. A. Nakajo, J. Kuebler, A. Faes, U.F. Vogt, H.J. Schindler, L.-K. Chiang, S. Modena, J. Van herle, T. Hocker, Compilation of mechanical properties for the structural analysis of solid oxide fuel cell stacks. constitutive materials of anode-supported cells. Ceram. Int. **38**(5), 3907–3927 (2012)

88. A. Nakajo, F. Mueller, J. Brouwer, J. Van herle, D. Favrat, Mechanical reliability and durability of SOFC stacks. Part I: modelling of the effect of operating conditions and design alternatives on the reliability. Int. J. Hydrogen Energy **37**(11), 9249–9268 (2012)

89. A. Nakajo, F. Mueller, J. Brouwer, J. Van herle, D. Favrat, Mechanical reliability and durability of SOFC stacks. Part II: modelling of mechanical failures during ageing and cycling. Int. J. Hydrogen Energy **37**(11), 9269–9286 (2012)

90. A. Nakajo, F. Mueller, J. Brouwer, J. Van herle, D. Favrat, Progressive activation of degradation processes in solid oxide fuel cells stacks: Part I: lifetime extension by optimisation of the operating conditions. J. Power Sources **216**(0), 449–463 (2012)

91. A. Nakajo, J. Van herle, D. Favrat, Sensitivity of stresses and failure mechanisms in SOFCs to the mechanical properties and geometry of the constitutive layers. Fuel Cells **11**(4), 537–552 (2011)

92. A. Nakajo, Z. Wuillemin, J. Van herle, D. Favrat, Simulation of thermal stresses in anode-supported solid oxide fuel cell stacks. Part I: probability of failure of the cells. J. Power Sources **193**(1), 203–215 (2009)

93. A. Nakajo, Z. Wuillemin, J. Van herle, D. Favrat, Simulation of thermal stresses in anode-supported solid oxide fuel cell stacks. Part II: loss of gas-tightness, electrical contact and thermal buckling. J. Power Sources **193**(1), 216–226 (2009)

94. N. Nemeth, J. Manderscheid, J. Gyekenyesi, Ceramics Analysis and Reliability Evaluation of Structures (CARES). Users and programmers manual (1990)

95. B. Nguyen, B. Koeppel, S. Ahzi, M. Khaleel, S. Prabhakar, Crack growth in solid oxide fuel cell materials: from discrete to continuum damage modeling. J. Am. Ceram. Soc. **89**(4), 1358–1368 (2006)

96. O.B. Olurin, D.S. Wilkinson, G.C. Weatherly, V. Paserin, J. Shu, Strength and ductility of as-plated and sintered CVD nickel foams. Compos. Sci. Technol. **63**(16), 2317–2329 (2003)

97. S.M. Oppenheimer, D.C Dunand, Finite element modeling of creep deformation in cellular metals. Acta Materialia **55**(11), 3825–3834 (2007)

98. K. Park, S. Yu, J. Bae, H. Kim, Y. Ko, Fast performance degradation of SOFC caused by cathode delamination in long-term testing. Int. J. Hydrogen Energy **35**(16), 8670–8677 (2010)

99. M. Pihlatie, H. Frandsen, A. Kaiser, M. Mogensen, Continuum mechanics simulations of NiO/Ni-YSZ composites during reduction and re-oxidation. J. Power Sources **195**(9), 2677–2690 (2010)

100. M. Pihlatie, A. Kaiser, M. Mogensen, Mechanical properties of NiO/Ni–YSZ composites depending on temperature, porosity and redox cycling. J. Eur. Ceram. Soc. **29**(9), 1657–1664 (2009)

101. M. Pihlatie, T. Ramos, A. Kaiser, Testing and improving the redox stability of Ni-based solid oxide fuel cells. J. Power Sources **193**(1), 322–330 (2009)

102. M. Radovic, E. Lara-Curzio, Mechanical properties of tape cast nickel-based anode materials for solid oxide fuel cells before and after reduction in hydrogen. Acta Materialia **52**(20), 5747–5756 (2004)

103. M. Radovic, E. Lara-Curzio, L. Riester, Comparison of different experimental techniques for determination of elastic properties of solids. Mater. Sci. Eng. A **368**(1–2), 56–70 (2004)

104. J.L. Routbort, K.C. Goretta, R.E. Cook, J. Wolfenstine, Deformation of perovskite electronic ceramics—a review. Solid State Ionics **129**(1–4), 53–62 (2000)

105. K. Sato, K. Yashiro, T. Kawada, H. Yugami, T. Hashida, J. Mizusaki, Fracture process of nonstoichiometric oxide based solid oxide fuel cell under oxidizing/reducing gradient conditions. J. Power Sources **195**(17), 5481–5486 (2010)

106. A. Selcuk, A. Atkinson, Elastic properties of ceramic oxides used in solid oxide fuel cells (SOFC). J. Eur. Ceram. Soc. **17**(12), 1523–1532 (1997)

107. A. Selimovic, M. Kemm, T. Torisson, M. Assadi, Steady state and transient thermal stress analysis in planar solid oxide fuel cells. J. Power Sources **145**(2), 463–469 (2005)

108. N. Shikazono, D. Kanno, K. Matsuzaki, H. Teshima, S. Sumino, N. Kasagi, Numerical assessment of SOFC anode polarization based on three-dimensional model microstructure reconstructed from FIB-SEM images. J. Electrochem. Soc. **157**(5), B665–B672 (2010)

109. D. Simwonis, F. Tietz, D. Stöver, Nickel coarsening in annealed Ni/8YSZ anode substrates for solid oxide fuel cells. Solid State Ionics **132**(3–4), 241–251 (2000)

110. E. Stephens, J. Vetrano, B. Koeppel, Y. Chou, X. Sun, M. Khaleel, Experimental characterization of glass-ceramic seal properties and their constitutive implementation in solid oxide fuel cell stack models. J. Power Sources **193**(2), 625–631 (2009)

111. C. Stiller, B. Thorud, O. Bolland, R. Kandepu, L. Imsland, Control strategy for a solid oxide fuel cell and gas turbine hybrid system. J. Power Sources **158**(1), 303–315 (2006)

112. B. Sun, R. Rudkin, A. Atkinson, Effect of thermal cycling on residual stress and curvature of anode-supported SOFCs. Fuel Cells **9**(6), 805–813 (2009)

113. Y. Suzue, N. Shikazono, N. Kasagi, Micro modeling of solid oxide fuel cell anode based on stochastic reconstruction. J. Power Sources **184**(1), 52–59 (2008)

114. R. Swindeman, M. Swindeman, A comparison of creep models for nickel base alloys for advanced energy systems. Int. J. Press. Vessels Pip. **85**(1–2), 72–79 (2008)

115. L.W. Tai, M.M. Nasrallah, H.U. Anderson, D.M. Sparlin, S.R. Sehlin, Structure and electrical properties of $La_{1-x}Sr_xCo_{1-y}Fe_yO_3$. Part 1. The system $La_{0.8}Sr_{0.2}Co_{1-y}Fe_yO_3$. Solid State Ionics **76**(3–4), 259–271 (1995)

116. L.W. Tai, M.M. Nasrallah, H.U. Anderson, D.M. Sparlin, S.R. Sehlin, Structure and electrical properties of $La_{1-x}Sr_xCo_{1-y}Fe_yO_3$. Part 2. The system $La_{1-x}Sr_xCo_{0.2}Fe_{0.8}O_3$. Solid State Ionics **76**(3–4), 273–283 (1995)

117. N. Takano, M. Zako, F. Kubo, K. Kimura, Microstructure-based stress analysis and evaluation for porous ceramics by homogenization method with digital image-based modeling. Int. J. Solids Struct. **40**(5), 1225–1242 (2003)

118. P. Tanasini, M. Cannarozzo, P. Costamagna, A. Faes, J. Van herle, A. Hessler-Wyser, C. Comninellis, Experimental and theoretical investigation of degradation mechanisms by particle coarsening in SOFC electrodes. Fuel Cells **9**(5), 740–752 (2009)

119. ThyssenKrupp. Material data sheet no. 4046.
120. F. Tietz, Thermal expansion of SOFC materials. Ionics **5**(1), 129–139 (1999)
121. S. Watanabe, F. Iguchi, J. Mizusaki, K. Sato, K. Yashiro, T. Kawada, Y. Takeyama, T. Hashida, Development of in-situ mechanical testing method for SOFC components. *Proceedings of the ASME 2010 Eigth International Fuel Cell Science*, 2010
122. W. Weibull, A statistical theory of the strength of materials. Proc. Roy. Swed. Inst. Eng. Res. **151**, 1–45 (1939)
123. K. Weil, J. Hardy, J. Rice, J. Kim, Brazing as a means of sealing ceramic membranes for use in advanced coal gasification processes. Fuel **85**(2), 156–162 (2006)
124. K. Weil, B. Koeppel, Comparative finite element analysis of the stress-strain states in three different bonded solid oxide fuel cell seal designs. J. Power Sources **180**(1), 343–353 (2008)
125. K. Weil, B. Koeppel, Thermal stress analysis of the planar SOFC bonded compliant seal design. Int. J. Hydrogen Energy **33**(14), 3976–3990 (2008)
126. K.S. Weil, C.A. Coyle, J.T. Darsell, G.G. Xia, J.S Hardy, Effects of thermal cycling and thermal aging on the hermeticity and strength of silver-copper oxide air-brazed seals. J. Power Sources **152**, 97–104 (2005)
127. K.S. Weil, C.A. Coyle, J.S. Hardy, J.Y. Kim, G.-G Xia, Alternative planar SOFC sealing concepts. Fuel Cells Bulletin **2004**(5), 11–16 (2004)
128. Z. Wuillemin, N. Autissier, A. Nakajo, M.-T. Luong, J. Van herle, D. Favrat, Modeling and study of the influence of sealing on a solid oxide fuel cell. J. Fuel Cell Sci. Technol. **5**(1), 011016–9 (2008)
129. H. Yakabe, Y. Baba, T. Sakurai, M. Satoh, I. Hirosawa, Y. Yoda, Evaluation of residual stresses in a SOFC stack. J. Power Sources **131**(1–2), 278–284 (2004)
130. H. Yakabe, Y. Baba, T. Sakurai, Y. Yoshitaka, Evaluation of the residual stress for anode-supported SOFCs. J. Power Sources **135**(1–2), 9–16 (2004)
131. H. Yakabe, I. Yasuda, Model analysis of the expansion behavior of $LaCrO_3$ interconnector under solid oxide fuel cell operation. J. Electrochem. Soc. **150**(1), A35–A45 (2003)
132. Z. Yang, M.S. Walker, P. Singh, J.W. Stevenson, T. Norby, Oxidation behavior of ferritic stainless steels under SOFC interconnect exposure conditions. J. Electrochem. Soc. **151**(12), B669–B678 (2004)
133. Z. Yang, K.S. Weil, D.M. Paxton, J.W Stevenson, Selection and evaluation of heat-resistant alloys for SOFC interconnect applications. J. Electrochem. Soc. **150**(9), A1188–A1201 (2003)
134. T. Zhang, Q. Zhu, W.L. Huang, Z. Xie, X. Xin, Stress field and failure probability analysis for the single cell of planar solid oxide fuel cells. J. Power Sources **182**(2), 540–545 (2008)